Determination of the Aeroelastic Transfer Functions for Streamlined Bodies by Means of a Navier-Stokes Solver

Davide Fransos*
Politecnico di Torino, Department of Mathematics
C.so Duca degli Abruzzi 24, I-10129, Torino, Italy
davide.fransos@polito.it

Luca Bruno
Politecnico di Torino, Department of Structural Engineering and Geotechnics
Viale Mattioli 39, I-10125, Torino, Italy
luca.bruno@polito.it

Abstract

This paper proposes a method to determine the flutter derivatives of 2-dimensional streamlined cylinders by means of a modified indicial approach adapted to a Navier-Stokes solver using an Arbitrary Lagrangian Eulerian formulation. The method relies on heave or pitch motion imposed to the section according to smoothed ramp time histories and on the computational evaluation of the transient forces arising on the obstacle. Hence, the indicial transfer function relating the plate motion with the induced force in the frequency domain is obtained. The application to a flat plate of finite thickness and length is proposed. The steady viscous flow simulated around the motionless plate is compared with the well-known Blasius solution. The computed flutter derivatives are compared both with the ones obtained from the Theodorsen function in the frame of the thin airfoil theory and with the ones resulting from previous methods in the frame of the computational approach.

Keywords: computational wind engineering, flutter, indicial approach, grid-based methods.

1 Introduction

The study of flutter instability of long, flexible structures is usually simplified by considering the two-dimensional (2D) airflow around a representative rigid section along the main span of the structure. The relationship between the aeroelastic force on section, induced by its own motion, and the motion itself can be expressed by an aeroelastic system characterized by transfer functions in frequency domain between input (motion) and output (force). It follows that this approach leads to a formulation of the aeroelastic system as a linear one. This assumption fully holds for streamlined bodies and allows to give the analytical expression of the transfer functions for 2D theoretical flat plate oscillating in potential flow (Theodorsen 1935 [1]).

On the other hand, this theory begins to fail in predicting the correct aeroelastic behavior of bluff bodies, for instance bridge cross sections. Their aerodynamics is basically driven by the separation of the boundary layer and its unsteady reattachment. Strictly speaking, the assumption about the linearity of the system no longer holds for such bodies. However, Scanlan & Tomko [2] firstly formulated a linearized model by assuming the same general format of the Theodorsen's analytical expression. The introduced empirical coefficients, the so-called flutter derivatives, have been related to the Theodorsen function in closed form for the streamlined flat plate by the same authors [3]. In case of bluff sections, such motional coefficients are generally obtained through wind-tunnel test on oscillatory section models (e.g. in Matsumoto [4]).

The computational calculation of these transfer functions is a challenging task for Computational Fluid Dynamics (CFD) and Computational Wind Engineering (CWE). In the last field of research, the most popular method to achieve this goal has been firstly proposed by Walther & Larsen [5] and successively applied to a

*Corresponding author – fax number: (+39) 011.564.7599.

number of bridge cross sections, e.g. in [6]. The method adopts sinusoidal imposed vibrations of the section in perfect analogy with the experimental tests. The moving boundaries of the fluid domain induced by the imposed oscillation are generally described in grid-based numerical methods by Arbitrary Lagrangian-Eulerian (ALE) formulation of the Navier-Stokes equations. The aerodynamic derivatives are obtained from the amplitude and phase relationships between the imposed motion and the fitted time histories of the aeroelastic force components. From a computational point of view, this method is very expensive because a time-dependent simulation is needed for every non-dimensional frequency (the so-called *reduced frequency*) of interest. Moreover, it requires that the extent of the simulated time histories of the aeroelastic force components is large enough to overcome the transient flow solution and to allow their correct fitting.

According to the authors, the above mentioned computational difficulties are not overcome in a recent study of Le Maître et al [7], in which an alternative method is proposed. The latter is based on spring-mounted airfoil placed in the free stream, subjected to an initial displacement and then let free to oscillate. The evaluation of the apparent damping ratios and apparent natural mechanical frequencies of the airfoil permits to determine the values of the flutter derivatives corresponding to the considered degree of freedom and reduced velocity. Once more, a simulation is needed for every reduced frequency of interest. Even if only the transient solution is of interest, its extent in time depends on the natural frequency of the mechanical system and in particular involves relevant computational costs at the lowest natural frequencies.

An alternative and promising method refers to the indicial approach successfully used by Wagner [8] to give the closed-form solution of the transient lift evolution versus time (the so-called Wagner indicial lift function) of a thin plate placed in a potential flow and subjected to a step-wise pitch motion. In order to recover the transfer function in frequency domain, the Theodorsen circulation function can be related to the Wagner function by the Fourier transform [9]. On one hand, the indicial approach is certainly less expensive from a computational point of view because of two main reasons. First, an unique simulation is needed to evaluate the transfer function in the whole range of interest of the reduced velocity. Second, only the transient flow is to be simulated and its extension in time does not depends on the structural natural frequency of the obstacle. On the other hand, great attention must be paid in order to make indicial approach compatible with the computational simulation of the flow. According to the authors, the first attempt made by Brar et al [10] to apply the indicial approach by means of CWE experienced some difficulties. In fact, in order to avoid the computational problems involved by the simulation of the motion of the obstacle, Brar et al assume that the relative angle of attack, associated to a vertical displacement of the section, can be equivalently simulated by a motionless obstacle subjected to impulsive initial condition, i.e. assuming an uniform velocity field in space at initial time. According to the authors, the above mentioned approach does not respect the physics of the transient flow nor eliminates the numerical errors due to the impulsive initial conditions. Such errors deeply affect the transient force arising on the structure just after the step-wise variation of the angle of attack of the flow. Hence, both the indicial function at its first time steps and its Fourier transform at high frequencies contain a non-physical contribution. Moreover, the proposed approach can not be extended to the pitch motion of the section. In another work applied to aircraft maneuvers, Lesieutre et al [11] simulate the motion of the wing using the more promising ALE approach. Furthermore, a smoothed-ramp motion of the section during a finite time is proposed in order to overcome the computational problems involved by the step-wise displacement and the infinite velocity of the structure.

The aim of the present work is to extend and adapt the above mentioned approach to the numerical calculation of the transfer functions between motion and force flutter derivatives in order to increase the accuracy and to reduce the required computational resources. The proposed method is applied to the flow around a thin plate subjected to heave or pitch smoothed ramp motion. A number of parametrical studies are devoted to optimize the parameters of the model and the computational procedures to assure the reliable simulations of the small scales in space and time resulting from the smoothed-ramp motion. The efficiency of the approach is discussed by comparing the obtained results with the closed form solution of the Theodorsen function, with the related flutter derivatives and with the computational results of Walter and Larsen.

2 Use of Indicial Theory with CWE codes

The method proposed herein in order to compute the 2D-flutter derivatives goes along the following steps:

1. computational simulation of the aerodynamic behaviour of the motionless obstacle with steady homogeneous incoming flow;

2. computational simulation of the effects of the motion of the obstacle in the flow:

(a) the motion (input $i(t)$) is prescribed according to a smoothed-ramp evolution in time;

(b) the resultant forces (output $o(t)$) are obtained by integration of the surface stresses on the body;

3. post processing in order to infer flutter derivatives from the simulated time histories of the input $i(t)$ and output $o(t)$ variables.

It is worth to point out that the method works for any kind of computational approach and physical model of the flow.

In the following, new proposals are detailed concerning the approach to recover the flutter derivatives (step 3.). Then, the analysis of the qualitative properties of several smoothed-ramp functions (step 2.) is carried out *a-priori* in order to select the most suitable ones in view of the their computational application. Finally, the effects of the ramp-time extension on the harmonic content of the selected input function are evaluated looking at the range of interest of the reduced velocity in wind engineering.

2.1 Recovering the aeroelastic transfer functions

In the following, a new approach is proposed in order to readily recover the 2-dimensional flutter derivatives from the time-histories of the body motion and of the acting forces obtained by computational simulation. Let us consider the expression of the aeroelastic forces resulting on an oscillating rigid body immersed in a 2D wind field given by the original model of Theodorsen [1]:

$$L = -\frac{1}{2}\rho U^2 B\,(2\pi)\left[\frac{B\dot{\theta}}{4U} + \frac{B\ddot{y}}{4U^2} + 2C(k)\Big(\theta + \frac{\dot{y}}{U} + \frac{B\dot{\theta}}{4U}\Big)\right], \tag{1}$$

and

$$M = -\frac{1}{2}\rho U^2 B^2\,(2\pi)\left[\frac{B\dot{\theta}}{16U} + \frac{B^2\ddot{\theta}}{128U^2} - C(k)\Big(\frac{\theta}{4} + \frac{\dot{y}}{4U} + \frac{B\dot{\theta}}{16U}\Big)\right], \tag{2}$$

while using the model by Scanlan & Tomko, reported in [3]:

$$L = \frac{1}{2}\rho U^2 B\Big[kH_1^*(k)\,\frac{\dot{y}}{U} + kH_2^*(k)\,\frac{B\dot{\theta}}{U} + k^2 H_3^*(k)\,\theta + k^2 H_4^*(k)\,\frac{y}{B}\Big], \tag{3}$$

and

$$M = \frac{1}{2}\rho U^2 B^2\Big[kA_1^*(k)\,\frac{\dot{y}}{U} + kA_2^*(k)\,\frac{B\dot{\theta}}{U} + k^2 A_3^*(k)\,\theta + k^2 A_4^*(k)\,\frac{y}{B}\Big], \tag{4}$$

where L and M are the lift force and the pitching moment evaluated at the pole $O\,(0.5B;0)$, B is the chord length of the body, U the unperturbed flow velocity, ρ the air density, y and θ respectively the heave and pitch component of the displacement of the pole O. Herein, the well known Theodorsen's circulation function $C(k) = F(k) + jG(k)$ and the so-called flutter derivatives $H_i^*(k)$ and $A_i^*(k)$ are expressed as function of the reduced frequency used in wind engineering practice $k = \omega B/U$, where $\omega = 2\pi n$ is the angular velocity of the body motion.

The aeroelastic system, because of the basic assumption of the model, can be seen as a linear map (Figure 1) between the input variables (displacements and velocities) and the output ones (aeroelastic forces). Hence,

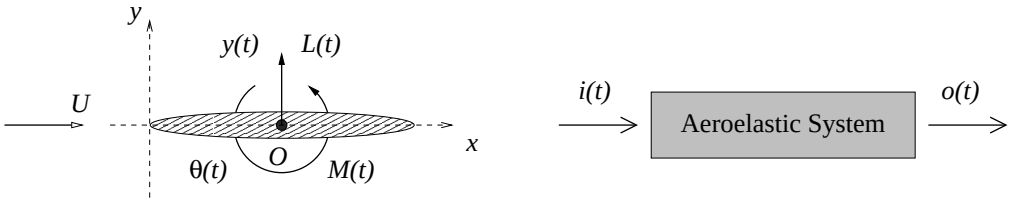

Figure 1: Aeroelastic forces on 2-dimensional cylinder

the expression 1 and 2 or the ones 3 and 4, obtained for sinusoidal motions, can be generalized to any kind of motion included the proposed smoothed ramp functions.

Let us consider a general evolution in time $\eta(t)$ of the input variable $\eta = i = y, \theta$ and the corresponding

time-history of the output variable in non dimensional form $\eta = o = C_L, C_M$ where $C_L = 2L/\rho U^2 B$ and $C_M = 2M/\rho U^2 B^2$. They can be expressed as the anti-transform of their Fourier transform:

$$\eta(t) = \mathcal{F}^{-1}\Big[\mathcal{F}[\eta(t)]\Big] = \int_{-\infty}^{+\infty} a_{\hat{\eta}}(\omega) e^{j(\omega t + \varphi_{\hat{\eta}}(\omega))} d\omega, \tag{5}$$

where $a_{\hat{\eta}}(\omega)$ and $\varphi_{\hat{\eta}}(\omega)$ are respectively the modulus and the phase angle of the Fourier transform of $\eta(t)$. Assuming a linear operator mapping input and output, for each reduced frequency k the argument of the integral in equation 5 can be expressed by means of equations 1- 2 or 3 - 4. For instance, let us consider $\theta(t)$ as input and $C_L(t)$ as output. One obtains by using the Theodorsen formulation:

$$a_{\hat{L}} e^{j(\omega t + \varphi_{\hat{L}})} = -\pi a_{\hat{\theta}} \Big[jk + 2C\Big(1 + \frac{1}{2} jk\Big)\Big] e^{j(\omega t + \varphi_{\hat{\theta}})}. \tag{6}$$

It follows that:

$$F + jG = -\frac{1}{\pi\,(2 + jk)} \Big[jk\pi + \frac{a_{\hat{L}}}{a_{\hat{\theta}}} e^{j(\varphi_{\hat{L}} - \varphi_{\hat{\theta}})} \Big]. \tag{7}$$

Analogously, referring to the formulation of Scanlan & Tomko, one obtains:

$$a_{\hat{L}} e^{j(\omega t + \varphi_{\hat{L}})} = \Big[kH_2^* \frac{B}{U} \frac{\mathrm{d}}{\mathrm{d}t} \Big(a_{\hat{\theta}} e^{j(\omega t + \varphi_{\hat{\theta}})} \Big) + k^2 H_3^* a_{\hat{\theta}} e^{j(\omega t + \varphi_{\hat{\theta}})} \Big] = k^2 a_{\hat{\theta}} \Big[jH_2^* + H_3^* \Big] e^{j(\omega t + \varphi_{\hat{\theta}})}. \tag{8}$$

It follows that:

$$H_3^* + jH_2^* = \frac{1}{k^2} \frac{a_{\hat{L}}}{a_{\hat{\theta}}} e^{j(\varphi_{\hat{L}} - \varphi_{\hat{\theta}})} = \frac{1}{k^2} \frac{a_{\hat{L}}}{a_{\hat{\theta}}} \Big(\cos(\varphi_{\hat{L}} - \varphi_{\hat{\theta}}) + j \sin(\varphi_{\hat{L}} - \varphi_{\hat{\theta}}) \Big), \tag{9}$$

and equating the real and imaginary components:

$$H_2^*(k) = \frac{1}{k^2} \frac{a_{\hat{L}}}{a_{\hat{\theta}}} \sin(\varphi_{\hat{L}} - \varphi_{\hat{\theta}}), \tag{10}$$

$$H_3^*(k) = \frac{1}{k^2} \frac{a_{\hat{L}}}{a_{\hat{\theta}}} \cos(\varphi_{\hat{L}} - \varphi_{\hat{\theta}}). \tag{11}$$

In an analogous manner the expressions of the remaining 6 flutter derivatives are easily obtained and listed in Tab. 2.1. The equation 7 or the ones 10 and 11 show that, whichever is the assumed engineering model, it

$$\begin{aligned}
A_1^*(k) &= \tfrac{B}{k^2} \frac{a_{\hat{M}}}{a_{\hat{y}}} \sin(\varphi_{\hat{M}} - \varphi_{\hat{y}}), \quad & H_1^*(k) &= \tfrac{B}{k^2} \frac{a_{\hat{L}}}{a_{\hat{y}}} \sin(\varphi_{\hat{L}} - \varphi_{\hat{y}}), \\
A_2^*(k) &= \tfrac{1}{k^2} \frac{a_{\hat{M}}}{a_{\hat{\theta}}} \sin(\varphi_{\hat{M}} - \varphi_{\hat{\theta}}), \quad & H_2^*(k) &= \tfrac{1}{k^2} \frac{a_{\hat{L}}}{a_{\hat{\theta}}} \sin(\varphi_{\hat{L}} - \varphi_{\hat{\theta}}), \\
A_3^*(k) &= \tfrac{1}{k^2} \frac{a_{\hat{M}}}{a_{\hat{\theta}}} \cos(\varphi_{\hat{M}} - \varphi_{\hat{\theta}}), \quad & H_3^*(k) &= \tfrac{1}{k^2} \frac{a_{\hat{L}}}{a_{\hat{\theta}}} \cos(\varphi_{\hat{L}} - \varphi_{\hat{\theta}}), \\
A_4^*(k) &= \tfrac{B}{k^2} \frac{a_{\hat{M}}}{a_{\hat{y}}} \cos(\varphi_{\hat{M}} - \varphi_{\hat{y}}), \quad & H_4^*(k) &= \tfrac{B}{k^2} \frac{a_{\hat{L}}}{a_{\hat{y}}} \cos(\varphi_{\hat{L}} - \varphi_{\hat{y}}).
\end{aligned}$$

Table 1: Expression of the flutter derivatives

is possible to determine the transfer function in the frequency domain for any input by evaluating the ratio between the Fourier transforms of output $o(t)$ and input $i(t)$, provided that the inverse of the latter is not singular. Furthermore, the modulus of the Fourier transform of input $a_{\hat{i}}(\omega)$ must be large enough with respect to the one of the output $a_{\hat{o}}(\omega)$ at every frequency of interest in order to guarantee the accurate numerical evaluation of the flutter derivatives. Finally, it is worth to point out that the method also applies to the classic Heaviside input function, where $a_{\hat{i}} = 1$ and $\varphi_{\hat{i}} = 0$.

2.2 Choice of the smoothed ramp function

In the indicial approach, the Heaviside or step-wise function is traditionally chosen as the input function $i(t)$ because the output function $o(t)$ is the indicial response function itself. In computational application a

step-wise variation of the imposed displacement cannot be exactly represented because of discretization errors. Moreover, its derivative versus time (velocity) shows large values generally involving nonphysical oscillations of the solution. Hence, a smoothed ramp is preferred. Two main guidelines must be taken into account in choosing the best smoothed ramped input.

First, the input represents a physic phenomenon continuous in time, so that an high class of continuity seems a reasonable choice. Lesieutre et al. [11] proposed a cosine function $f_{sin}(t)$ and a 5th order polynomial one $f_{p5}(t)$:

$$f_{sin}(t) = \begin{cases} 0 & t < t_0 \\ \frac{a_i}{2}\Big[1 - cos\Big(\frac{\pi}{T_r}t\Big)\Big] & t_0 \le t \le T_r \\ a_i & t > T_r \end{cases} , \tag{12}$$

$$f_{p5}(t) = \begin{cases} 0 & t < t_0 \\ \frac{a_i}{T_r^3}\Big[10t^3 - \frac{15}{T_r}t^4 + \frac{6}{T_r^2}t^5\Big] & t_0 \le t \le T_r \\ a_i & t > T_r \end{cases} , \tag{13}$$

where a_i is the amplitude of the ramp reached after an elapsed "ramp time" T_r from the start at $t = t_0$. It is worth to point out that both functions are defined piecewise. Moreover, using the function $f_{sin}(t)$, the input is defined in $C^1(\mathbb{R})$: it follows that its second derivative, i.e. the acceleration of the motion, is discontinuous in $t = 0$ and $t = T_r$. Using functions $f_{p5}(t)$, the input is defined in $C^2(\mathbb{R})$, so that both velocity and acceleration are continuous. In order to guarantee the highest class of continuity, the error function is proposed in the present study:

$$f_{erf}(t) = \frac{a_i}{2}\Big[1 + erf(b(t-c))\Big], \quad -\infty \le t \le +\infty \ . \tag{14}$$

Bearing in mind that $f_{erf} \in C^\infty(\mathbb{R})$ and that its derivatives have a Fourier transform of the form $(i\omega)^n \hat{f}_{erf}(\omega)$, where n is the order of the derivative, any of them can be adopted as the input time-history. In the following, the first derivative, i.e. the Gaussian function, is employed in order to smooth the Dirac function instead of the Heaviside one:

$$f_{gau}(t) = a_i e^{-(b(t-c))^2}, \quad -\infty \le t \le +\infty \ . \tag{15}$$

The start time and the ramp-time for the last two functions are respectively defined as $t_0 \,|\, i = 0.01a_i$ and $t_0 + T_r \,|\, i = 0.99a_i$ because of their asymptotic trend to initial and final values.

The second guideline refers to the harmonic content of the input function. In fact, as expressions in Table 2.1 clearly shows, special attention must be paid in order to assure a significant harmonic content at the upper bound of the range of the reduced frequency k, or correspondingly at the lower one of the range of the reduced velocity $U_r = U/nB$. The functions described above, their first-order derivatives versus time and the normalized harmonic content of the latter are plotted in Figure 2 adopting the same ramp-time T_r. Looking at the functions smoothing the step-wise one, $f_{erf}(t)$ is characterized by the steepest evolution around $T_r/2$ for a given T_r: hence, its frequency content is extended at higher frequencies than the ones of $f_{p5}(t)$ and f_{sin}. Conversely, the functions show comparable harmonic contents when the ramp-time is chosen in order to obtain the same maximum value of their derivatives, as clearly shown in Figure 3. It follows that even if the displacement is usually adopted as input variable, in the present study the performances of the functions illustrated above are computationally evaluated for a common value of the maximum angular velocity.

Finally, it is worth to point out that the harmonic contents of the error and Gaussian functions do not show oscillations due to the numerical procedures adopted to transform the signal. Hence, an high class of continuity of the function seems to be preferred because it does not require special care in the numerical post-processing.

2.3 Choice of the ramp time

The ramp time T_r must be short enough to assure a significant harmonic content at high values of the reduced frequency k or equivalently at low values of the reduced velocity $U_r = U/nB$. The ramp time T_r for f_{erf}

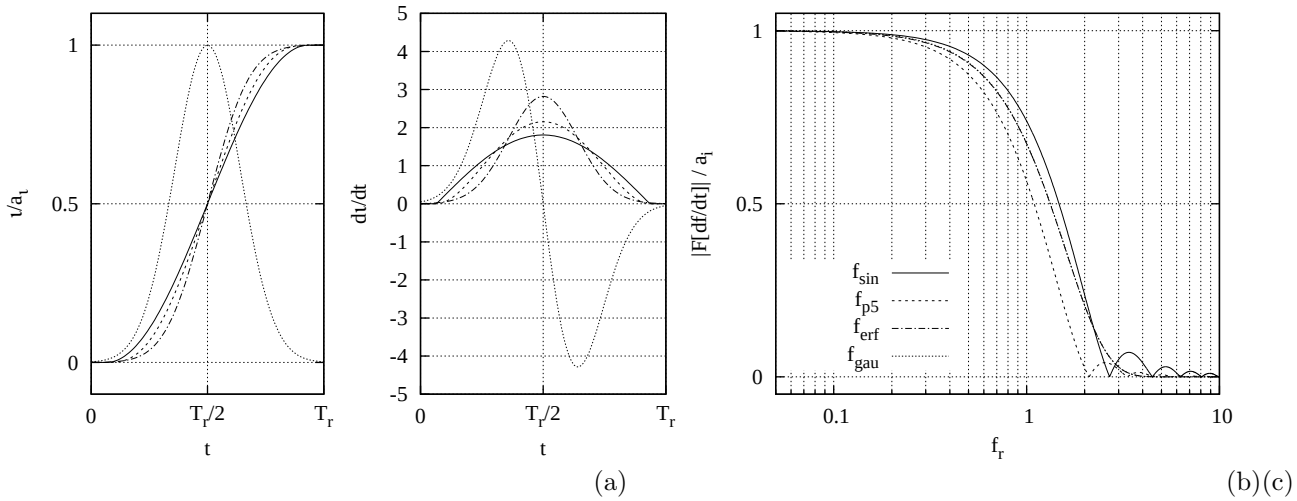

Figure 2: Ramp functions (a), first order derivatives (b) and normalized harmonic content (c) with same ramp time ($T_r = 8.7e-1$)

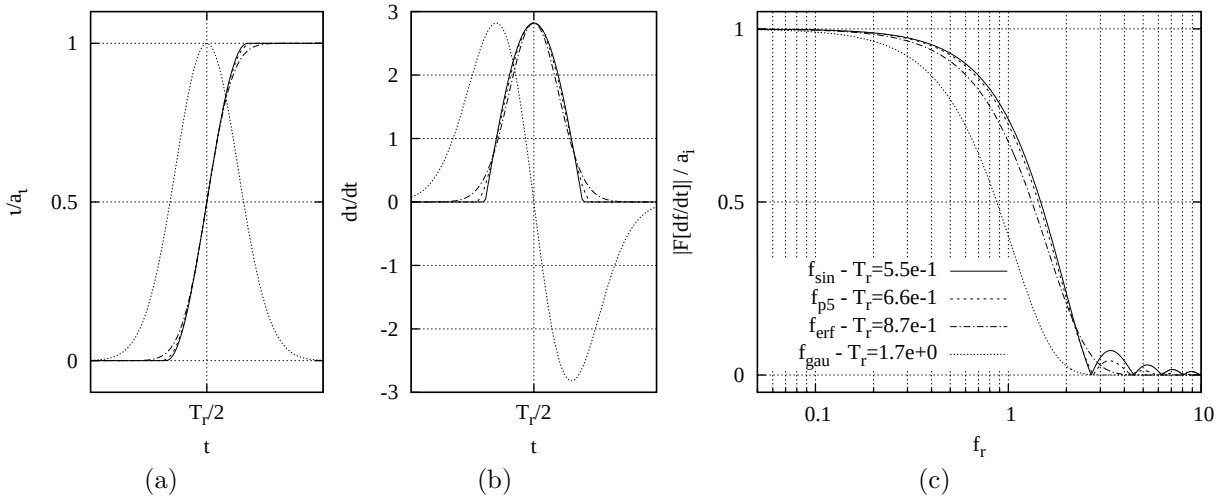

Figure 3: Ramp functions (a), first order derivatives (b) and normalized harmonic content (c) with same maximum velocity $max\,(di/dt)$

can be modified varying the parameter b. Its harmonic content is plotted in Figure 4 for different values of T_r. The threshold value of the harmonic content of the input i can be hardly set *a priori*. First, as eqns. 10 - 11 clearly show, the accurate evaluation of the flutter derivatives depends from the ratio $a_{\hat{o}}(w)/a_{\hat{i}}(w)$ and not only from $a_{\hat{i}}(w)$. Second, the above mentioned threshold value depends from the numerical error introduced both in the computational simulation of the flow and by the numerical treatment of the results during post-processing. A trail value of $0.1a_{\hat{i}}$ is assumed. Hence, bearing in mind that generally in wind engineering $0.2 \leq Ur \leq 12$, $b = 5$ and $T_r e - 1$ can be adopted (Fig. 4). The adequacy of this ramp time will be verified during the results discussion, once the output evolution is simulated.

3 Governing Equations and Computational Approach

Computational simulation of fluid-structure interaction problems is a challenging task that can be performed through different approaches, depending on the type of interaction and the aim of the simulation. In this paper, the solid structure sub-system is modeled as a 2D-SDOF rigid body and its dynamics is fully described by the imposed displacemet $i(t)$ of its rotational center. The coupled fluid-structure system is then reduced to a fluid flow in a time-dependent domain, and the motion of the domain boundary is known *a priori*. Time-dependence of the domain introduces a further requirement for grid-based numerical methods, i.e. an efficient

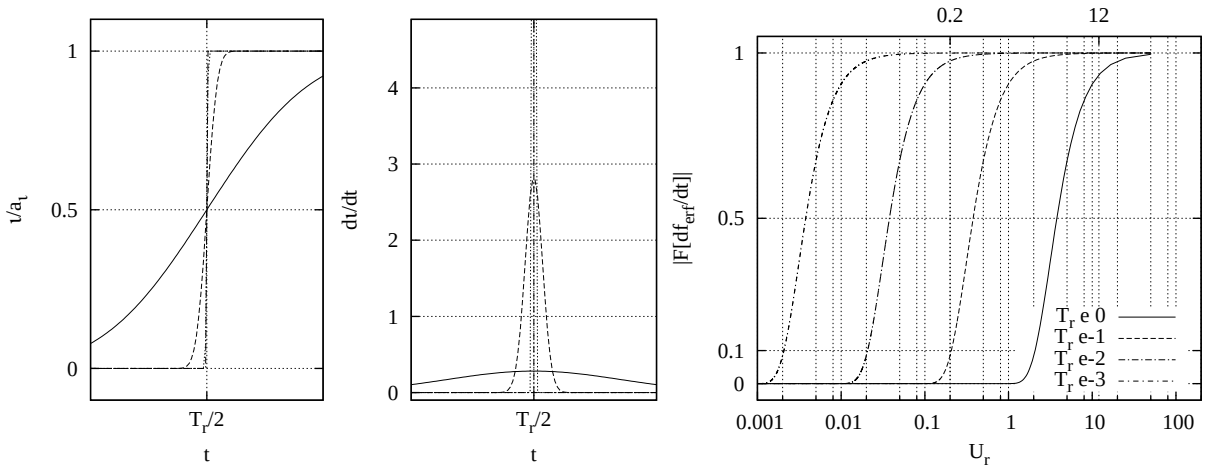

Figure 4: Erf ramp function (a), first order derivatives (b) and normalized harmonic content at different ramp times T_r

way to move the computational grid.

The function $f = i(t)$ has been discussed in detail in the previous paragraphs. Next paragraphs are devoted to describe the mathematical modelling of the fluid flow system, the moving grid strategy and the numerical method employed for solving the obtained model.

3.1 Flow modelling

The incompressible, unsteady, two-dimensional laminar flow with moving boundaries is modeled in the present study by means of the Navier-Stokes equations. For a moving domain $\Omega_f(t)$, the Arbitrary Lagrangian Eulerian approach (ALE, [12] [13]) allows to introduce a reference frame $\hat{\Omega}_f$, which is mapped for each time t into the fluid domain by $\xi \mapsto \mathbf{x}(t, \xi)$, where ξ and $\mathbf{x}$ are respectively the ALE and Eulerian (spatial) coordinates. The classical nondimensional instantaneous continuity and momentum equations are then modified into their ALE counterpart expressed in terms of the fluid variables relative to the moving frame

$$\begin{cases} \operatorname{div} \mathbf{u} = 0, & \mathbf{x} \in \ \Omega_f(t), \ t > 0, \\ \left.\dfrac{\partial \mathbf{u}}{\partial t}\right|_{\xi} + (\mathbf{u} - \mathbf{u}_g) \operatorname{grad} \mathbf{u} = -\operatorname{grad} p + \dfrac{1}{Re} \Delta \mathbf{u}, & \mathbf{x} \in \ \Omega_f(t), \ t > 0, \end{cases} \tag{16}$$

where $\mathbf{u}$ is the velocity of the fluid, $\partial(\cdot)/\partial t\big|_{\xi}$ the time derivative on the ALE frame, $\mathbf{u}_g = \partial \mathbf{x}/\partial t\big|_{\xi}$ the frame velocity, p the pressure, $Re = UB/\nu$ the Reynolds number, ν the kinematic viscosity of the air. The boundary motion is then treated imposing

$$\mathbf{u}_g = \frac{\partial \mathbf{x}}{\partial t}, \quad \forall \mathbf{x} \in \ \partial\Omega_f(t), \ t > 0, \tag{17}$$

and solving an auxiliary problem in order to determine $\mathbf{u}_g$ inside the domain. The choice of an appropriate auxiliary problem characterize the ALE method; the choice adopted in this work is described in paragraph 3.2.

The conditions imposed on the external boundaries of the domain $\Omega_f(t)$ are Dirichlet ones on velocity at inlet and Neumann ones on the normal component of the stress tensor at outlet, as depicted in figure 5(a).

Noting that the classical Eulerian form of the Navier-Stokes equations can be recovered, in absence of boundary motion, imposing $\mathbf{u}_g = 0$, such a choice is adopted for simulating the flow around motionless obstacle in junction with no-slip boundary conditions at wall

$$\mathbf{u} = \mathbf{u}_g = 0, \quad \mathbf{x} \in \ \Gamma_s, \ t > 0, \tag{18}$$

and impulsive initial conditions

$$\mathbf{u}^0 = (U, V), \quad \mathbf{x} \in \ \Omega_f, \ t = 0. \tag{19}$$

The more general Arbitrary Lagrangian Eulerian approach (eq. 16) is used for simulations with moving obstacle in junction with the corresponding form of the no-slip boundary condition at wall

$$\mathbf{u} = \mathbf{u}_g(t) = \mathbf{u}_w\left(\mathbf{i}(t)\right), \quad \mathbf{x} \in \ \Gamma_s, \ t > 0, \tag{20}$$

where $\mathbf{u}_w\left(\mathbf{i}(t)\right)$ is the wall velocity corresponding to the imposed input obstacle motion $\mathbf{i}(t)$. The velocity field simulated around the motionless obstacle is used as initial condition for the flow velocity field in moving obstacle problems.

3.2 Grid generation strategy

In the grid-based methods, two main goals are pursued concerning the mesh in simulating flow problems with moving boundaries. First, the minimization of the computational cost required to adapt the grid to the changes in the domain geometry; second, the maximization of the grid quality at each time step. The grid-generation procedures available in literature differ from the goal mainly pursued and from the their field of application. In order to define it, the ratio $a_i/\Lambda_{\mathbf{x}}$ between the maximum body displacement a_i and the characteristic length of the grid cell $\Lambda_{\mathbf{x}}$ can be assumed as a significant parameter. Hence, the choice among the options is strongly problem-dependent.

On one hand, the application forwarded in this paper involves small displacements of the solid boundary coherently with the assumption of the Scanlan's model ($a_i \approx Be-2$). On the hother hand, it calls for very fine meshes in order to accurately solve the thin viscous boundary layer at high Re numbers (e.g. $a_i/\Lambda_{\mathbf{x}} \approx 1e+2$ at $Re = 1e+4$). Moreover, the simulation of the unsteady aerodynamics of the moving obstacle requires high grid quality in its neighborhood and in its wake.

The most general procedure implies a body-conforming mesh that has to be regenerated at each time-step by changing the grid topology: its high computational cost is justified only in case of large boundary displacements ($a_i \approx Be+1$) as in some aeronautic applications (e.g. the store separation problem in [14]).

The linear interpolation of the original block-wise structured grid is widely used in Computational Wind Engineering [6] [15] [16], because the grid connectivity is maintained and the computational cost due to node replacement is low. Nevertheless, for high value of the $a_i/\Lambda_{\mathbf{x}}$ ratio, the interpolated grid generally shows non-orthogonal, skewed cells in the most dense regions. Hence, a significant amount of numerical diffusion can be introduced [17]. Moreover, the grid generation around obstacles with complex geometries, even if possible, involves a relevant number of nodes and hence increased costs.

The deformation of the existing unstructured grid is usually referred to as a "dynamic mesh" approach according to the early work of Batina [18]. The approach represents an excellent compromise between the above mentioned goals at moderate values of the boundary displacement ($a_i \approx B$). In this paper, the spring analogy method is adopted in order to deform the dynamic mesh. The grid is viewed as a quasi-static pseudo-structural discrete system. In this analogy, a fictitious lineal spring is attached along each edge connecting two vertices i and j of the fluid mesh, and the stiffness coefficient of this spring is chosen to be inversely proportional to the length l_{ij}^n of the supporting edge at each time-station t^n

$$k_{ij}^n \propto \frac{1}{l_{ij}^n}. \tag{21}$$

Then, the position of the dynamic mesh is obtained from the solution of the quasi-static problem

$$\begin{cases} \mathbf{K}^n\mathbf{q}^n = 0, & \xi_i \in \ \Omega_g, \\ \mathbf{q}^n = \overline{\mathbf{q}}^n, & \xi_i \in \ \Gamma_s, \\ \mathbf{q}^n = 0, & \xi_i \in \ \Gamma_g, \end{cases} \tag{22}$$

where $\mathbf{K}^n$ is the current stiffness matrix associated with the fictitious lineal springs, $\mathbf{q}^n$ is the current displacement vector whose terms are defined by

$$q_i^n = \xi_i^n - \xi_i^0\,, \tag{23}$$

$\overline{\mathbf{q}}^n$ denotes the prescribed displacement vector of the moving boundary Γ_s of the solid domain Ω_g, Ω_g the deformed domain and Γ_g its fixed outer boundary. The value of k_{ij}^n given in Eq. 21 is motivated by the fact that if it happens that during the mesh motion two vertices get closer, the lineal spring attached to the edge connecting the vertices becomes stiffer and therefore prevents them from colliding. Nevertheless, this method often results in invalid triangulations due to grid lines crossovers in case of triangular cells with high aspect

ratio. Moreover, the spring analogy can not be applied to quadrangular cells, especially required in boundary layer discretization because of their quality. In order to cope with the above mentioned difficulty, several proposals have been formulated in the last years (e.g. in [19] within the framework of the spring method). In this paper, the artificial field Ω_g of the computational grid is furtherely partitioned by means of a II level decomposition in three sub-field (Fig. 5(b)) analogously to what has been done in [6] and [16]. An hybrid

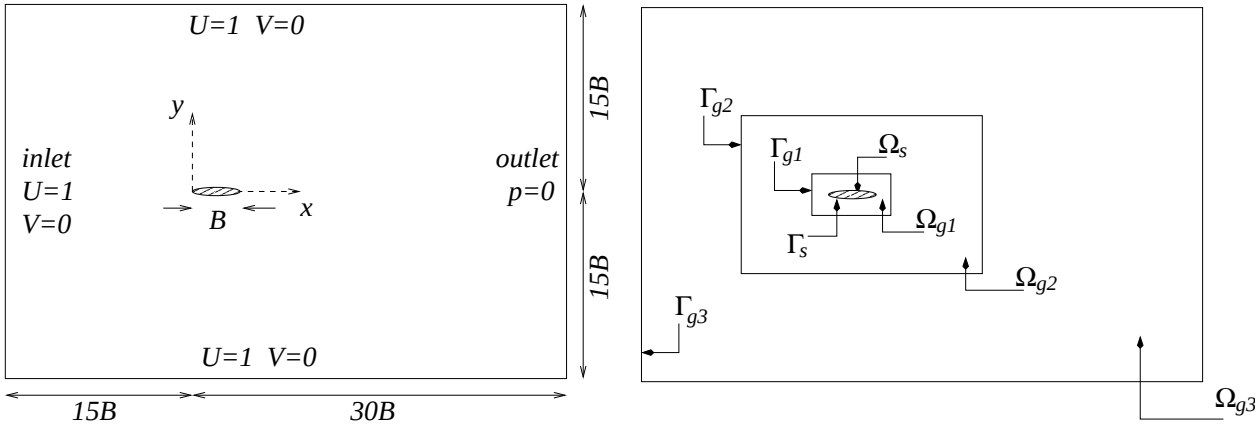

Figure 5: Computational domain, boundary conditions (a) and partitions for ALE approach (b)

adaptive quad/tri grid approach is adopted to discretize the resulting complex computational domain. A body-fitted, structured quadrangular grid is generated near the wall in partition Ω_{g1} in order to guarantee the best initial grid quality with orthogonal and unskewed cells. A triangular grid is generated to cover the intermediate domain Ω_{g2} using an advancing front method. Finally, a coarse paved quad grid is used to fill the outer domain Ω_{g3}.

The structured quad grid around solid boundary Γ_f moves with the moving body, while the paved one remains stationary. Meanwhile, the unstructured triangular grid is deformed to bridge from the imposed displacements on Γ_{g1} to the zero-displacements on Γ_{g2}.

$$\begin{cases} \mathbf{q}^n = y^n + \theta^n \mathbf{r}, & \xi_i \in \Gamma_s\,, \Omega_{g1}\,, \Gamma_{g1}, \\ \mathbf{q}^n \text{ from eq. (17)}, & \xi_i \in \Omega_{g2}, \\ \mathbf{q}^n = 0, & \xi_i \in \Gamma_{g2}\,, \Omega_{g3}\,, \Gamma_{g3}, \end{cases} \tag{24}$$

where $\mathbf{r}$ is the distance between the $i-th$ vertex and the center of rotation O.

Because the quad grids are not deformed, their quality remains the same along the simulation, which is especially a benefit for solving the viscous boundary layer. In addition, the outer sub-domain Ω_{g3} does not require re-meshing procedures, reducing the computational cost.

3.3 Numerical method

Computations were performed by the FLUENT 6.2 code, based on the Finite Volume Method. General literature on Finite Element and Finite Volume methods can be found in [20], [21], [22] and [23].

The physics of the investigated flow seems to be significantly sensitive both to numerical diffusion effects (affecting the smoothing of the velocity defect in the wake of the streamlined obstacle and the small vortical structures induced by its motion) and to numerical dispersion effects (i.e., it appears to cause phase errors between the obstacle displacements and the motion-induced forces acting on it). It is worthy to observe that the higher is the Reynolds number of the flow, the lower are the diffusive effects due to cinematic viscosity and the more relevant is the numerical diffusion. Thus, the computational simulation of flows characterized by high Reynolds numbers is very sensitive to numerical errors. Advancement in time is accomplished by the 1st order implicit Euler scheme. The cell-center values of the variables are interpolated at faces locations using a second order Central Difference Scheme for the diffusive terms and by means of a Quadratic Upwind Interpolation for Convective Kinematics (QUICK) for the convection terms. The local order and the overall leading error made on the flux of a generic variable ϕ by the above mentioned schemes are summarized in Table 3.3. The space interpolation is evaluated on a Cartesian equispaced grid for the pure convection equation. Because of

term	scheme	local order	overall leading error	main effect
time	Euler impl.	1st	$\Delta t/2\left(d^2\phi/dt^2\right)$	diffusive
convective	QUICK	3rd	$\Delta x^2/24\left(\partial^3\phi/\partial x^3\right)$	dispersive

Table 2: Adopted numerical scheme

the dependency of the leading errors to the grid spacing Dx, various Dx are tested. The pressure-velocity coupling is achieved by means of the pressure-implicit PISO algorithm, using a predictor-corrector approach for the time discretization of the momentum equation, whilst enforcing the continuity equation.

4 Application and results

The proposed approach is applied to the parallel incoming laminar flow along a finite-length smooth flat plate at a relatively high Reynolds number $Re_B = 1.e+4$. A finite thickness $D = B/400$ and rounded leading and trailing edges are adopted to obtain a streamlined section. According to the boundary layer theory [24], the transition from the laminar boundary layer to the turbulent one (occurring at $Re_{x,crit} =\approx 3.e+6$) does not take place under the above mentioned conditions. Furthermore, the boundary layer separation is avoided for fixed plate at moderate angle of attack α and for moving plate at small velocities of the wall. Hence, the formulation of the aeroelastic system as a linear one is fully adequate. Moreover, the flow conditions allow the comparison with the results obtained in closed form by Blasius, as reported by Schlichting [24], and Goldstein [25] for the steady plate and in the frame of the thin airfoil theory [1] for the oscillating plate.

From the computational point of view, every simulation in the following is obtained by using the same computational domain. The extension of the latter and the conditions applied at its outer boundaries are depicted in Figure 5(a).

Apart from to the grid-generation strategy illustrated above, the density of the control volumes (cv) is mainly dictated by two problem-dependent aspects. First, the finest grid is obtained in the neighborhood of the obstacle by imposing a cell thickness close to the wall $y_w = 5.e-6B$ in order to accurately resolve the laminar wall boundary layer.

Even if the accurate simulation of the flow in the neighborhood of the plate plays a dominant role in steady aerodynamics, an analogous precision is required in predicting the velocity distribution in the wake in view of the study of the aeroelastic behavior. In fact, the indicial response quantifies the effect on the aeroelastic forces of perturbations of the flow field induced by impulsive motion and then convected far from the obstacle in its wake. Hence, the accurate computational simulation of the transport mechanisms (convection and diffusion) along the wake plays a relevant role in predicting flutter derivatives at high reduced velocities. The effects of the grid density in the wake region on the computational results are discussed by taking into account three grid systems. They differ in the extension of the finer grid down-wind the trailing edge of the plate and they will be designated in what follows respectively by grid 1, grid 2 and grid 3 (see Table 4). The cross-wind

name	t_w	l_w	cv number	refined region
grid 1	$0.2B$	$0.001B$	3.0e+4	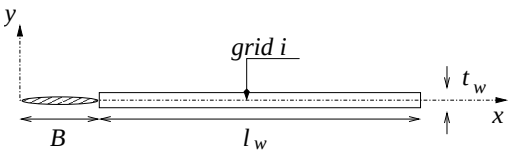
grid 2	$0.2B$	$1B$	5.3e+4	
grid 3	$0.2B$	$8B$	10.5e+4	

Table 3: Adopted computational grids

dimension t_w of the region down-wind the trailing edge is kept equal to $0.2B$ while its along-wind extension l_w varies according to the values reported in the same Table. The region down-wind the trailing edge is characterized by a non-dimensional control volume (cv) surface approximatively equal to $A_{cv}/B^2 = 1.e-4$. The outer part of the computational domain retains the same grid. The performance of these three systems is first evaluated in junction with fixed obstacle and then with moving plate.

4.1 Steady-state flow past the fixed plate

The simulation of the aerodynamic behaviour of the fixed plate in steady viscous flow is preliminarily accomplished in order to validate the computational model with respect to the well known exact solutions of Blasius and Goldstein [24] and to provide suitable initial condition for the simulation with moving obstacle. The velocity field around the plate obtained from the actual computational solution is compared in figure 6 with the Blasius closed-form one and with the computational results obtained by Walther & Larsen [5]. The

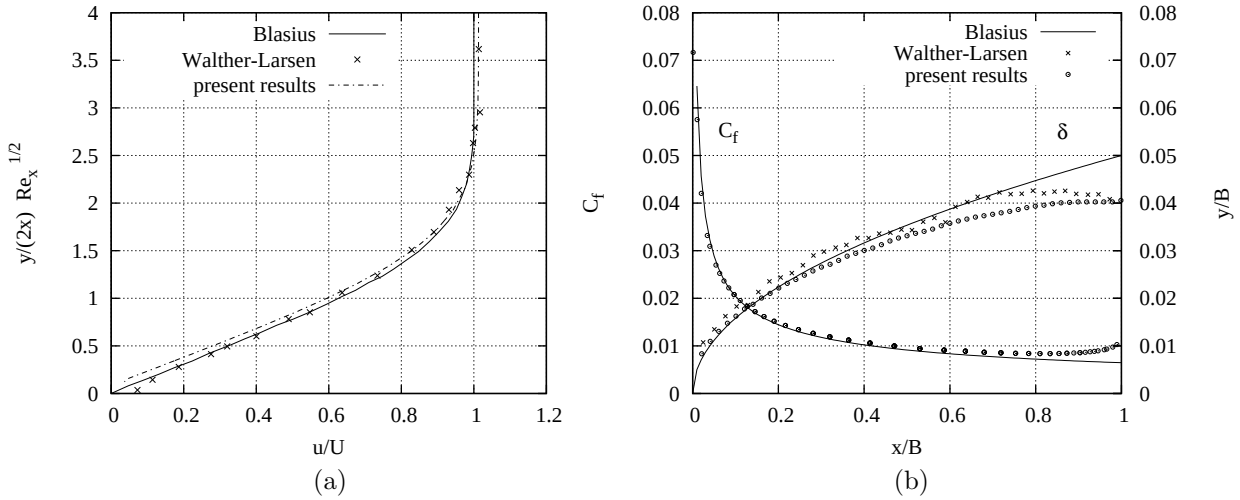

Figure 6: Steady-state flow past the plate: velocity profile at $x/B = 0.5$ (a), boundary layer thickness δ and friction coefficient C_f (b)

velocity profile in the boundary layer at $x/B = 0.5$ (Fig. 6a) and the evolution of the boundary layer thickness δ ($\delta = y/B \,|\, u = 0.99U$) and of the friction coefficient C_f along the profile (Fig. 6b) show a good overall agreement with the closed form solution. The reduced agreement between results in the neighborhood of the trailing edge ($x/B \geq 0.8$) is probably due to the finite length and thickness of the actual plate in contrast to the Blasius' assumptions. The error made in overestimating the value of the drag coefficient C_D is less than 7% with respect to the Blasius solution $C_D = 2\left(1.328\sqrt{Re_B}\right)$, coherently with the differences pointed out in the friction coefficient distribution.

Even if the simulated flow in the neighborhood of the plate shows satisfying accuracy for engineering purposes in steady aerodynamics, the same precision is required in predicting the velocity distribution in the wake in view of the study of the aeroelastic behaviour. In order to make it clearer,it is useful to refer to the relationship between the indicial function and the flutter derivatives: the former measures the effects on the aeroelastic forces of perturbations of the flow field, induced by the impulsive motion of the obstacle and then driven in its wake. Hence, the accurate computational simulation of the transport mechanisms (convection and diffusion) along the wake plays a relevant role in predicting flutter derivatives at high reduced velocities.

The streamwise velocity profiles at the trailing edge ($1.0B$) and at three locations in the wake ($1.005B$, $1.5B$ and $7.5B$) are compared in Figure 7 with the exact solution provided by Goldstein [25] and some experimental data collected by Acrivos et al [26].

First, it is worth to point out the relevant effect the grid spacing acts on the across-wind extent of the wake and on the velocity defect. In fact, an overall accuracy is obtained with every grid in the neighborhood of the trailing edge; the numerical diffusion involved by the spacing in grid 2 excessively smooths the velocity gradient at $x/B = 1.5$; only the grid 3 correctly simulates the velocity defect at $x/B = 7.5$.

Second, the velocity defect in the neighbourhood of y/B = 0 for $x/B \leq 1.0135$ obtained by every computational model is deeper than the one predicted in closed form (Fig. 7 (a)-(b)). Once more, this result is due to the finite thickness of the modeled plate in contrast with the Blasius' assumption. To prove this, a further computational simulation has been performed assuming a thin plate ($B/D = \infty$) and a grid characterized by the same density of grid 3. The streamwise velocity distribution obtained with the thick and thin plate are compared in Figure 8. It is clear that the effects of the thickness ($D = 2.5e-3B$) on the wake are significant at a distance from the trailing edge equal to $De + 1$ (Fig. 8(a)), while at a distance of half a chord they are almost negligible.

Finally, the evolution of the streamwise velocity along the centerline is plotted in Figure 9(a) for the three

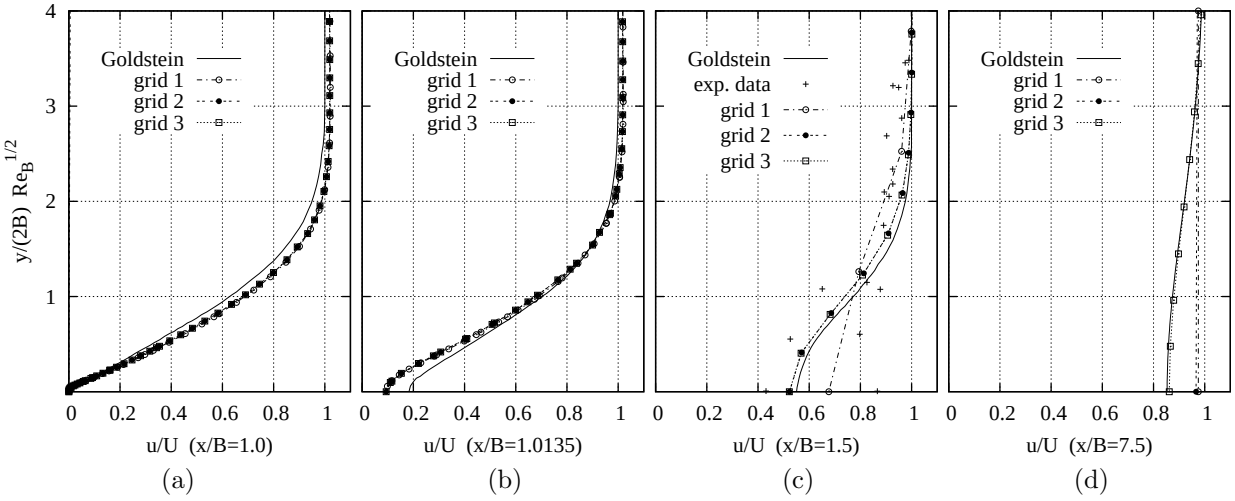

Figure 7: Streamwise velocity distribution along four straights across the wake

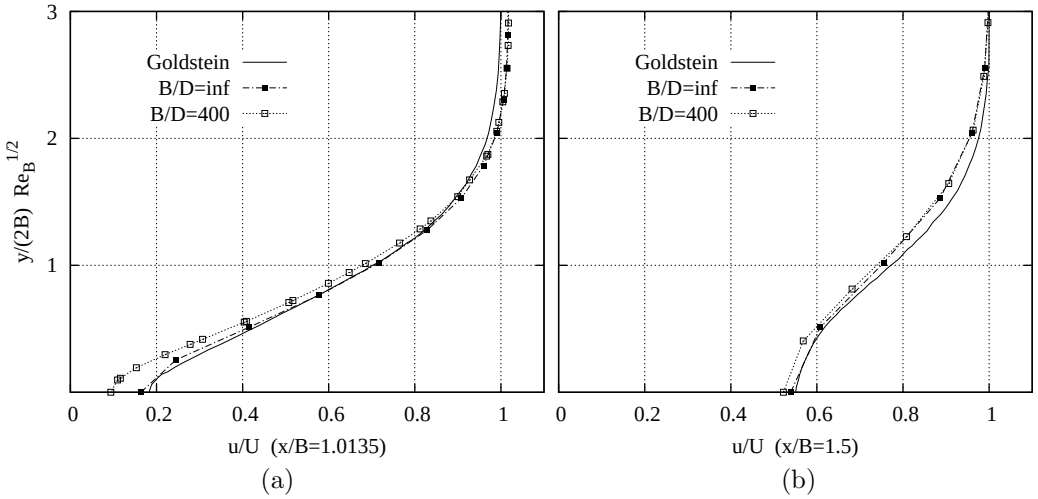

Figure 8: Streamwise velocity distribution in the wake of thick ($B/D = 400$) and thin ($B/D = \infty$) plate

computational grids and the Goldstein solution. In order to establish a relationship between the accuracy of the solution in the wake and the cv surface, the latter is plotted in Figure 9(b) for the same grids. It is clear that the lack of accuracy corresponds to the coarsening of the grid for every model. For the present flow conditions, a cv characteristic length of $1e-2B$ seems to guarantee an high accuracy in junction with quad cv and with the adopted numerical schemes.

4.2 Recovering the aeroelastic transfer functions

The computational simulation of the unsteady flow is performed assuming a time step $\Delta s = 1e-3$, where $s = tU/B$ is the non dimensional time unit. High discretization density in time is required to provide an accurate description of the ramped motion along $T_r = 0.87s$ and in order to reduce the diffusive effect of the truncation error involved by the EUL-1 scheme. The amplitude of the prescribed smoothed ramp is chosen in order to fulfill the assumption of small displacements according to the thin airfoil theory. Hence $a_\theta = +1^\circ$ (counterclock wise) is adopted for the pitch rotation around the torsional axis at the mid-chord of the plate. Then, the heaving amplitude is fixed in order to obtain the same maximum wall velocity at the tips of the plate, i.e. $a_y = +8.7e-3B$.

In what follows, an example of the results in the time and frequency domains is given. It is obtained by applying step-by-step the proposed approach for $i = \theta$ and $o = C_L$. Figure 10(a) compares the evolution in time of θ and $d\theta/dt$ imposed in the proposed approach and in the indicial theory. In figure 10(b) the same

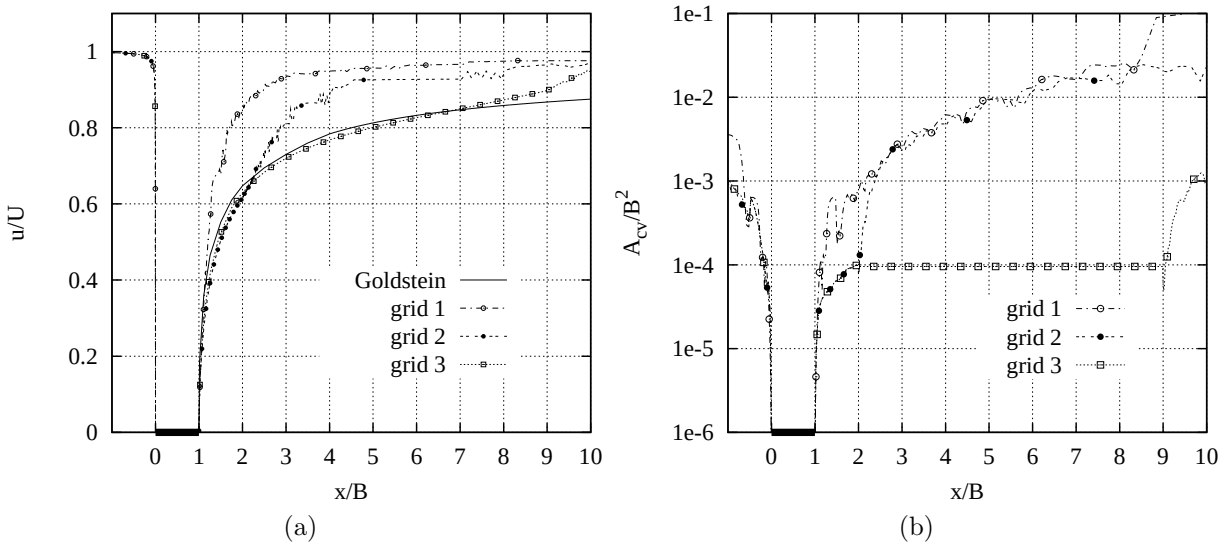

Figure 9: Streamwise velocity distribution (a) and cv surface (b) along the centerline

comparison is made between the normalized lift coefficient obtained by computational simulation and the one predicted in closed form (Wagner function). Figure 10 clearly shows the dependency of the lift evolution to

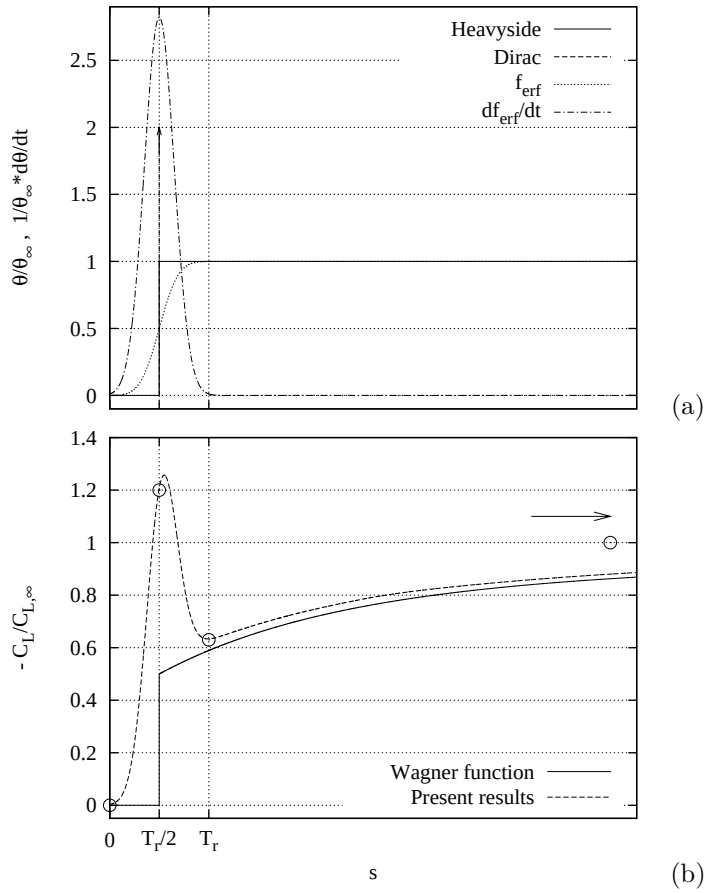

Figure 10: Comparison between evolution in time of θ, $d\theta/dt$ and C_L according to analytical solution and computational results

the rate on change of the pitching angle during the motion of the obstacle ($0 \leq t \leq T_r$). From a physical point

of view, around $T_r/2$ the velocity of the wall plays a dominant role in determining the velocity field around the obstacle, hence the pressure distribution around it.

In order to point out these effects, figure 11 shows the instantaneous pressure coefficient distribution along the upper and lower surfaces of the plate corresponding to the normalized C_L values pointed out by a circle in figure 10(b). The C_p distribution does not change from $t = 0$ ($\theta = 0°$) to $t = \infty$ ($\theta = 1°$) in a regular way, i.e. as if the displacement were quasi-static (see curve "quasi-static $\theta = 0.5°$" i.e. with $d\theta \backslash dt \approx 0$). In fact, at $t = T_r/2$ ($\theta = 0.5°$ with $d\theta/dt \neq 0$) the transient C_p distribution does not lay between the limit curves, but it shows, around the mid-chord, motion-induced higher pressure and suction respectively at upper and lower surfaces.

At $t = T_r$ the velocity of the wall falls to zero but the lift coefficient does not behave in the same way

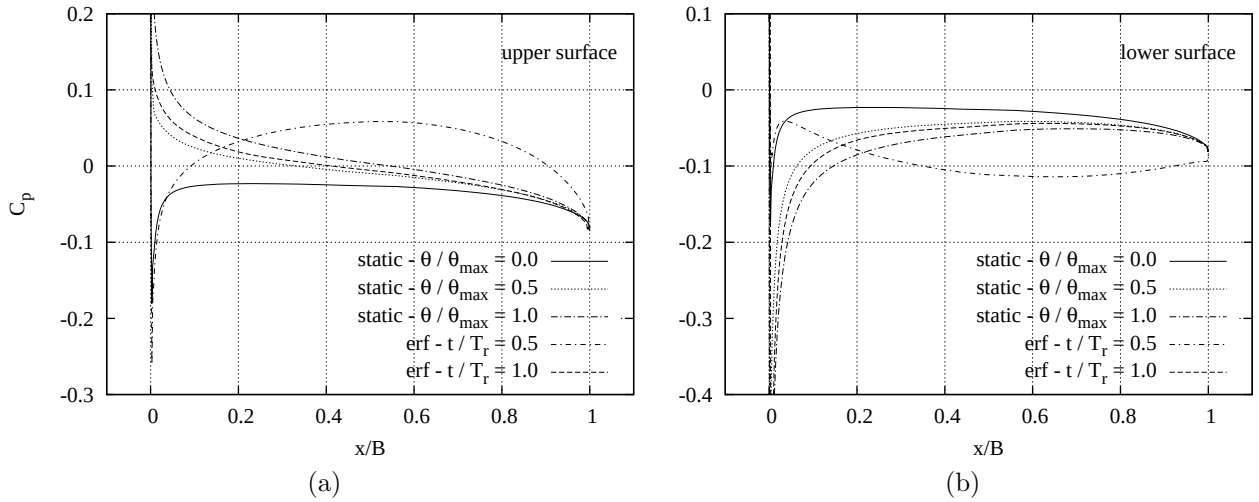

Figure 11: Evolution of the pressure coefficient distribution at upper (a) and lower (b) surface

because of the change in the angle of attack of the flow. For $t > T_r$ the flow field perturbed by the velocity of the wall is transported in the wake of the obstacle by convective and diffusive effects. The common asymptotic trend of the curves describes this phenomenon.

Finally, the real and imaginary parts of the Theodorsen function and the flutter derivatives relating pitching motion and lift coefficient are respectively shown in figure 12(a) and (b). The ones obtained by the computational simulation throughout equations 7 and 10 - 11 are compared with the closed form solutions. It

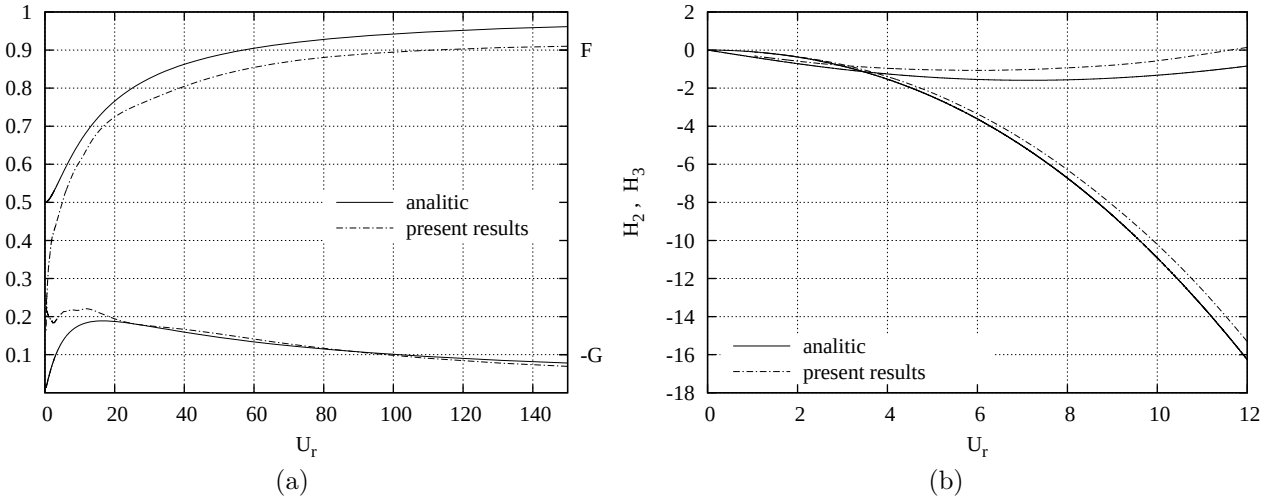

Figure 12: Comparison between aeroelastic transfer functions from analytical solutions and computational results

is worth to point out that the evident discrepancies for $t < T_r$ between the Wagner function and the computed

lift time-history have no significant effect on the corresponding flutter derivatives H_2^* and H_3^*. In fact, as the above mentioned equations clearly show, both the ratio of the modulus and the difference of phases of the Fourier transform of θ and C_L allow to normalize the output with respect to the given input.

4.3 Parametrical study on the ramp functions

A parametrical study on different types of ramp functions is carried on in order to evaluate computationally their properties, yet checked *a-priori* in par. 2.2, and to select the most appropriate one to be kept in the rest of the study. In accordance with the partial conclusions of the above mentioned paragraph, the parameters of each function are chosen in order to obtain the same maximum wall velocity during the motion of the obstacle.

The Figure 13 shows the evolution in time of the normalized lift and moment coefficients as a consequence of the different imposed motions. Two main differences between the aerodynamic responses are worth to

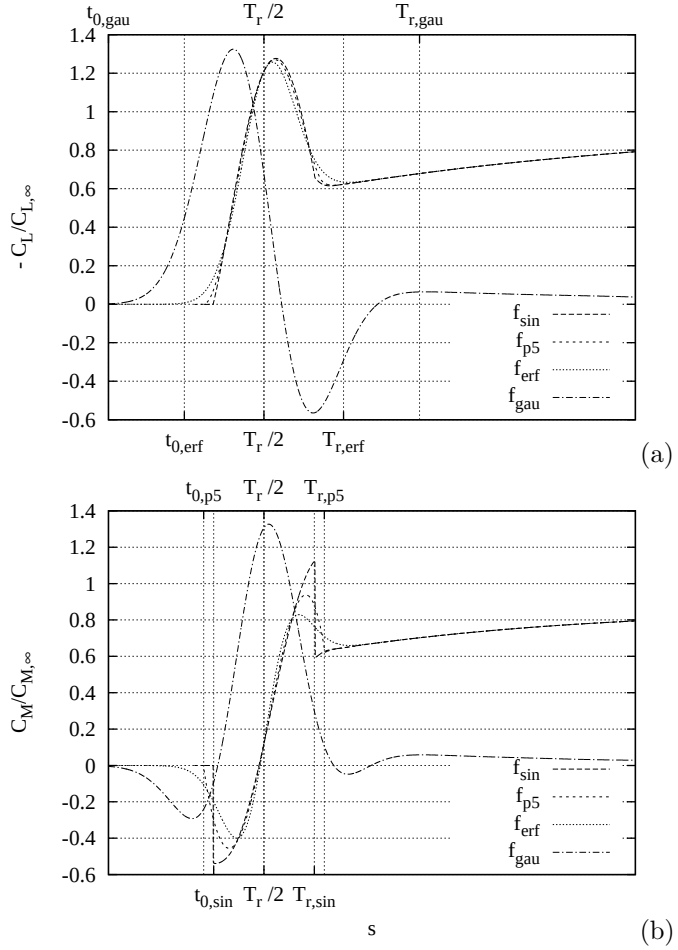

Figure 13: Comparison between the evolution in time of C_L and C_M face to different ramp functions

be remarked. First, the Gaussian ramp leads to an asymptotic behaviour different from the others ramps; lift and moment coefficient go back to their initial values, because of the recovered initial incidence of the obstacle.

Second, the time-history of the moment coefficient obtained by the sinusoidal ramp (Figure 13(b)) shows two jumps at the initial ($s = T_{0,sin}$) and at the final time ($s = T_{r,sin}$) of the motion. Let us recall (par. 2.2) that the sinusoidal function is defined in C^1. Hence, the above mentioned jumps are probably related to the discontinuity in the velocity profile of the ramped motion. In order to enforce this hypothesis by looking at the physics of the flow, the instantaneous C_p distribution along the upper and lower surfaces is plotted in figure 14 at the timesteps before (t_{n-1}) and after (t_{n-1}) the maximum angular velocity of the profile. The pressure distribution caused by the error function erf shows a minor variation both at upper and lower surface. On

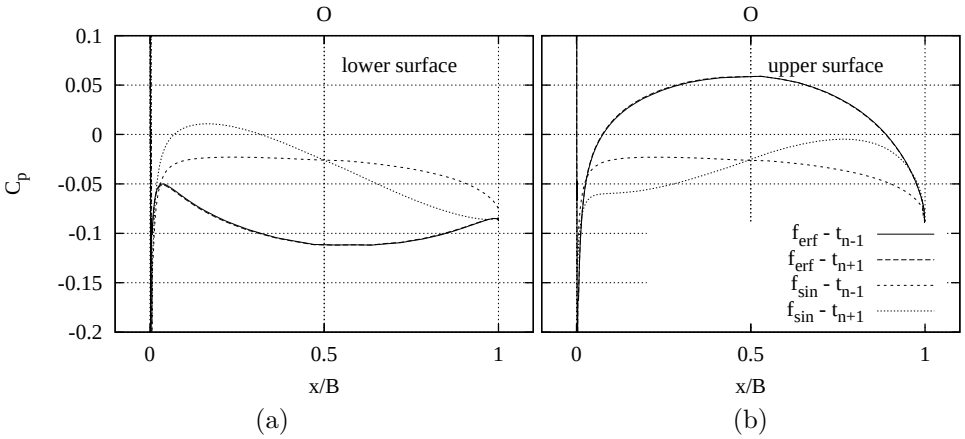

Figure 14: Evolution of the C_p distribution at upper (a) and lower (b) surface face to f_{sin} and f_{erf}

the contrary, the sinusoidal ramp involves relevant changes in the C_p distribution during only one timestep. For both functions, only the pressure at the rotation point O (tangential velocity of the wall equal to zero) remains the same. It is worth to point out that, in spite of such changes in C_p for the sin ramp, only the moment coefficient shows discontinuities, while the lift one is characterized by smooth evolution. In order to explain this difference, the wall is divided in four regions, upper left and right and lower left and right, and the C_p is integrated over each one of these. The resulting forces applied at the aerodynamic center $(O_i|M = 0)$ of each region are shown in Figure 15. Let us focus our attention on the effect of the sinusoidal function

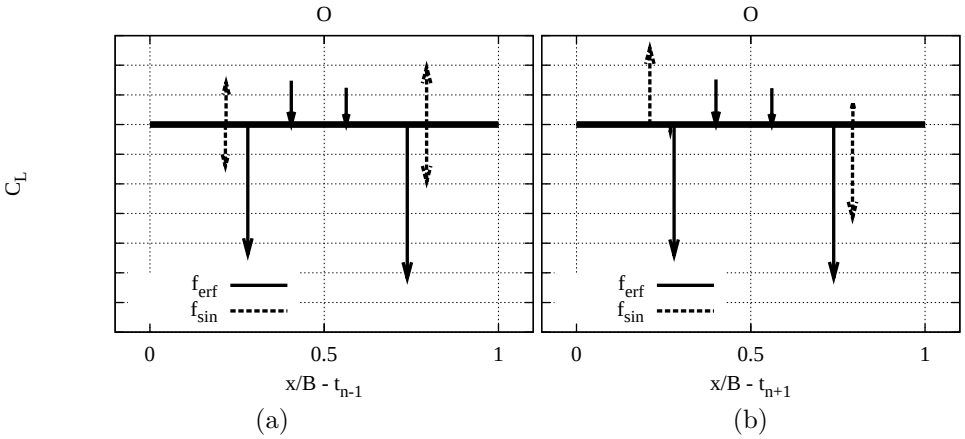

Figure 15: Lift components acting on the body before (a) and after (b) the maximum acceleration

(dotted vectors). On one hand, in the upper left and in the lower right regions the forces increase, while in the other two regions they decrease. On the other hand, the two negative and the two positive components of the variation have a compensation. Finally, the aerodynamic centers do not significantly move from one time step to the following one. Hence, this leads to a relevant variation in the only moment coefficient and not in the lift coefficient.

Figure 16 shows the flutter derivatives obtained by the simulations with different ramp functions. It is worth to point out that the above mentioned differences in the moment coefficient behaviour for the sinusoidal function previously mentioned lead to a worst computation of the derivatives coming from the moment coefficient itself ($A2$ and $A3$). It is also important to remark that the other ramp functions lead to an almost equivalent computation of the derivatives, except from the erf function that seems to give a better prediction of the $A2$ derivative. Generally speaking, these results confirm that an higher class of continuity is best suited for the input ramp, coherently with what stated in the *a-priori* analysis.

Because of the above-mentioned results, the error function is retained in the following.

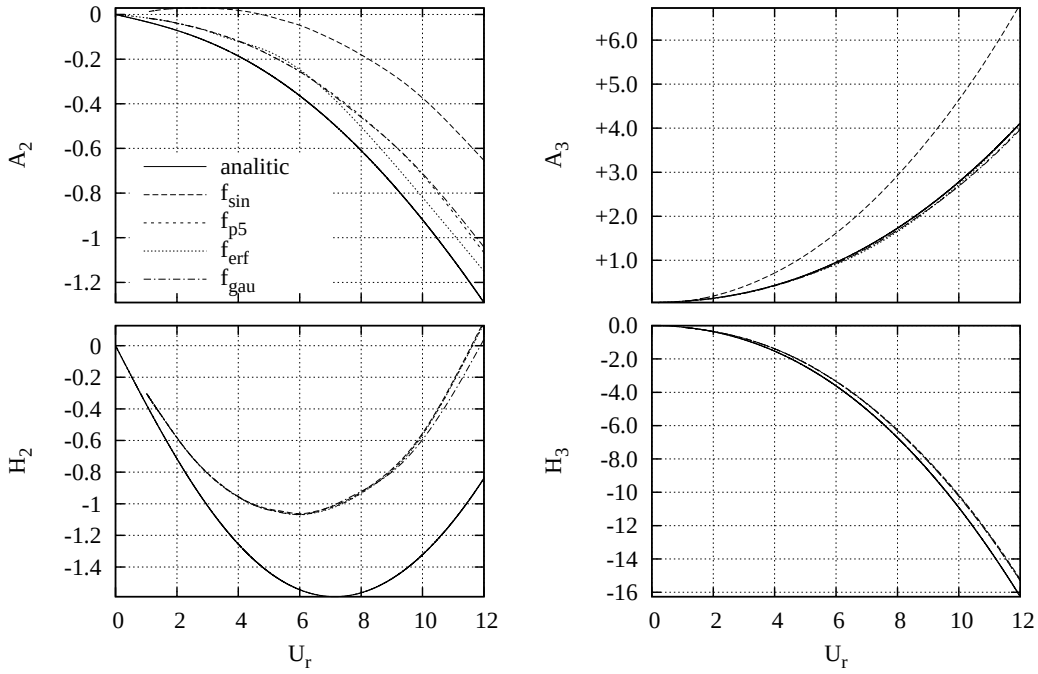

Figure 16: Flutter derivatives obtained with different ramp functions

4.4 Parametrical study on the ramp time

The error function is adopted as the ramp one in the rest of the analysis. The research of the best suited input function is completed by a parametrical study on the extension of the ramp time T_r.

In order to introduce the reasons of the study, it is worth to point out from Figure 10 that, for $T_r \to 0$, the ramped motion and the system response in time tend to the theoretical ones (Heaviside and Wagner functions). The same trend holds in frequency domain: in fact, as stated in paragraph 2.2, the ramp time must be short enough in order to assure the appropriate harmonic content of the input at the lower bound of the range of interest of the reduced velocities (i.e. at the upper one of frequencies). Hence, from the point of view of the system dynamics it can be supposed that the smaller is T_r, the better is the agreement between the computational and the closed form solutions.

Nevertheless, the reduction of the ramp time also involves unwished effects. From the aerodynamic point of view, the boundary layer separation can be expected in case of excessive values of $d\theta/dt$ and high velocity magnitude of the wall at the leading and trailing edges. Hence, the linearity hypothesis on the aeroelastic system no longer holds. From the computational point of view, the discretization in time of the motion requires the ratio $T_r/\Delta t$ to be fixed (in this work $T_r/\Delta t \approx 1000$) in order to guarantee accuracy. Hence, the smaller is T_r, the higher is the computational cost of the simulation. Finally, other difficulties can arise in postprocessing by numerically evaluating the Fourier transform of input and output in case of small Dt and long time-traces.

The same ramp time $T_r = 0.87s$ as used in 4.2 is assumed as the reference ramp time. Then, smoothed ramp motions with the ramp times $T_r = 8.7e-i\ s,\ i = 0, 1, 2, 3$ are taken into account for the rotational d.o.f.

Figure 17 shows the evolution of the aerodynamic coefficients obtained with simulations performed with the above mentioned ramp times and plotted versus the normalized non-dimensional time s/T_r. For $T_r = 8.7e0s$, $T_r = 8.7e-1s$ and $T_r = 8.7e-2s$, the lift and moment coefficient profiles show an analogous behaviour. It can be split in a first part mainly driven by the velocity of the motion of the obstacle (see 4.2) and in a second part affected by the no longer zero angle-of-attack. In both parts the lift coefficient remains positive. On the contrary, for $T_r = 8.7e-3s$, the lift coefficient profile shows one oscillation more than the previous ones, with a local negative minimum. The analysis of the instantaneous distributions of the x-friction coefficient $C_{f,x}$ can help to better understand the physical reasons of the lift behaviour. The distributions corresponding to the local maxima/minima during $0 \le s \le T_r$ for $T_r = 8.7e-1s$ and $T_r = 8.7e-3s$ (circles in Fig. 17) are compared between them and with the static case in Figure 18. The static solution is characterized at both angles of attack by a positive values of $C_{f,x}$ and a maximum point located at the

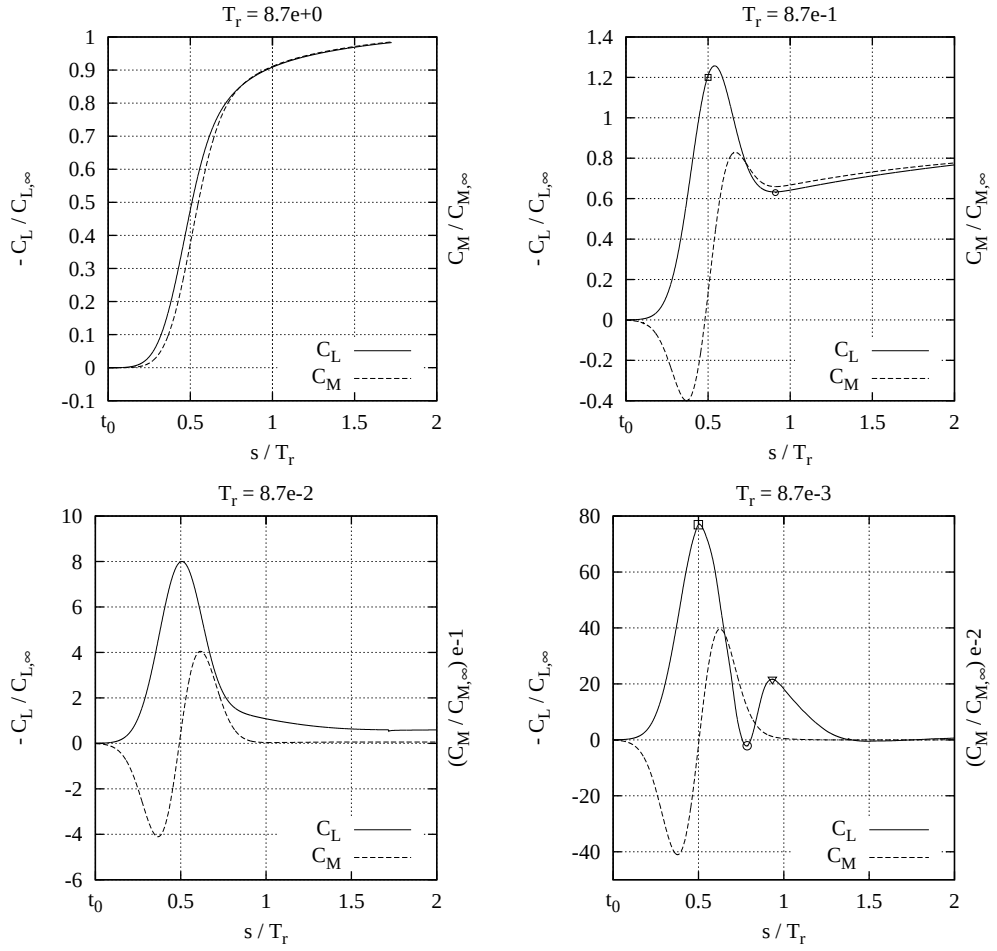

Figure 17: Comparison between the evolution in time of C_L and C_M face to different ramp times

rounded leading edge. Also the longer ramp time avoids negative values of the x-friction coefficient, i.e. backward flow and boundary layer separation. Nevertheless, the flow is deeply affected by the velocity of the wall, as the local maximum in the neighborhood of the leading edge on the lower surface witnesses. Finally, it can be seen that at $T_r/2$ the shorter ramp time involves negative values of $C_{f,x}$ in the neighborhood of the leading and trailing edge on the upper surface and around the center of rotation on the lower surface. It follows that local backward flow and boundary layer separation characterize the flow during the motion of the plate. Hence, the smoothed ramp motion with the ramp time $T_r = 8.7e-3$ is discarded in the rest of the paper.

Finally, in order to find a good compromise between harmonic content, acceptable costs and coherent flow regime, let us observe the computed flutter derivatives for the remaining T_r (fig. 19). When $T_r = 8.7e0$ is used, every flutter derivative shows large oscillations at $U_r < 3$, i.e. in the range of interest of the Wind Engineering. Such oscillations take place for a given reduced velocity when the harmonic content of input and output is less or equal to the order of magnitude of the errors made along the whole numerical procedure. These difficulties are tackled by using $T_r = 8.7e-1$: the oscillations rise up to higher frequencies, i.e. they are shifted in the range of reduced velocity $U_r \leq 0.2$ having no relevance for practical applications in Wind Engineering. Shorter ramp times (e.g. $T_r = 8.7e-2$) guarantee the same result but the computational efficiency decreases because the computational costs mentioned above grow up. Hence, a ramp time $T_r = 8.7e-1$ is held in the following.

4.5 Parametrical study on the grid density in the wake

The influence of the accurate simulation of the flow in the wake on the aeroelastic behavior of the plate is investigated in this section. From a qualitative point of view, the motion of the obstacle is expected to perturb

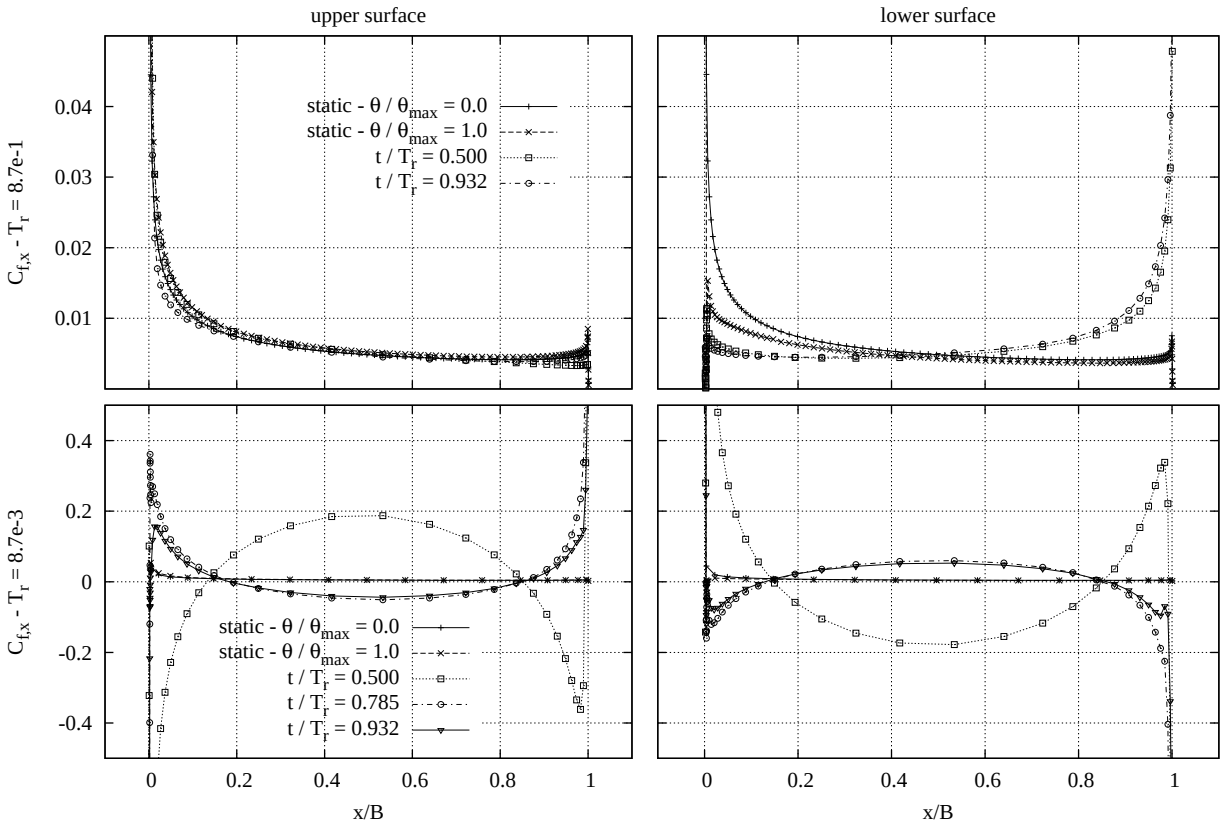

Figure 18: Evolution of the x-friction coefficient distribution at upper (a) and lower (b) surfaces

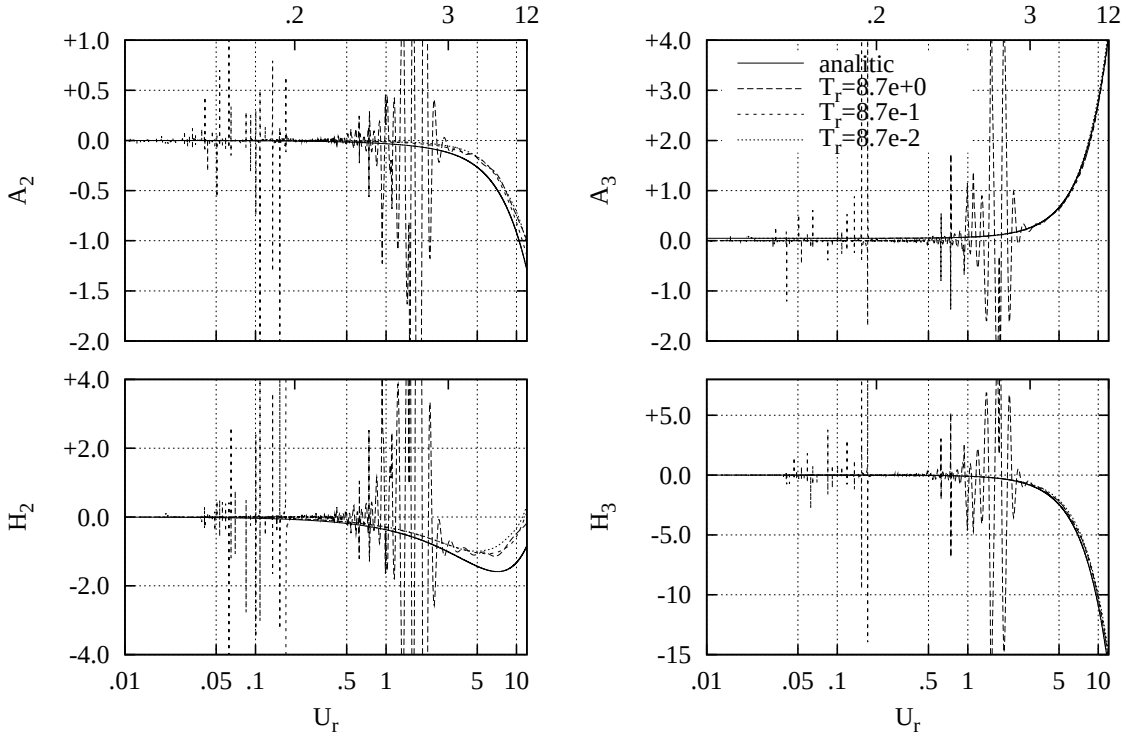

Figure 19: Flutter derivatives obtained with different ramp times

the velocity field around the leading edge. Then, this perturbation is transported in the wake by convection and diffusion mechanisms, so that it is expected to move along the wake far from the obstacle and to become weaker and weaker. It is worth to remind that the roles played by convection and diffusion are summarized by the Reynolds number and that the latter is generally high in both aeronautical and wind engineering applications. Hence, attention must be paid to avoid the introduction of an excessive amount of numerical diffusion with respect to the physical one in the computational solution. In order to gain some guidelines about this aspect, the smoothed ramp characterized by error function, $T_r = 8.7e-1$ and rotational d.o.f. is carried out on the three different grids introduced in 4. Figure 20 shows the cross-velocity in the wake, along the line $y/B = 0$, at several times from $s = T_r/2 + 0.5$ up to $s = T_r/2 + 8.5$ with a sampling interval equal to $\Delta s = 1$. The counterclock-wise rotation of the plate involves the pulling up of the leading edge and hence

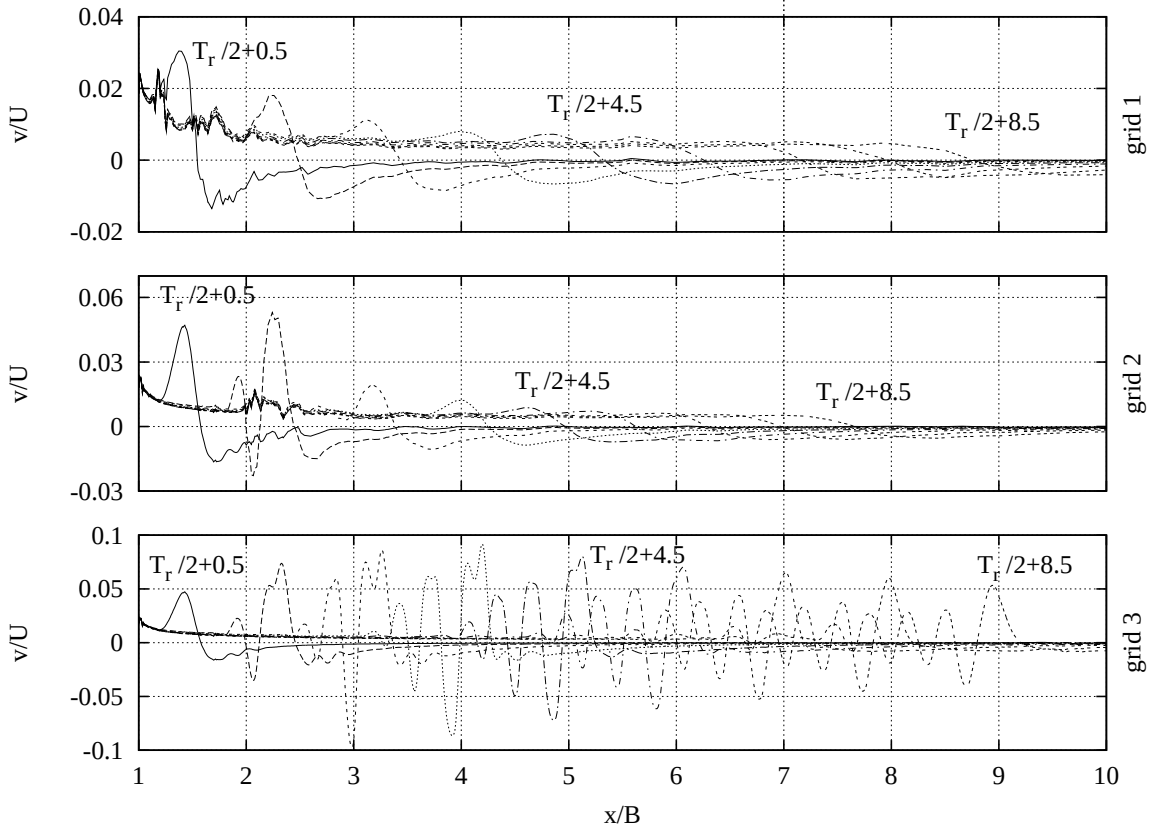

Figure 20: Transverse velocity in the wake with different grid density

the cross component v of the flow velocity is no longer equal to zero near it. In other words, a vortex is shed from the trailing edge and transported in the wake. Let us assume a velocity of convection downstream the plate of the same order of magnitude of the one of the undisturbed flow ($U = 1$) because of the extremely thin wake. Hence, at the above mentioned times, the core of the vortex (i.e. where $v/U = 0$) is roughly expected to be placed respectively at $x/B = 1.5$ and $x/B = 9.5$.

The perturbation on v for grid 1 is affected by a very rapid decay, starting yet from $s = T_r/2 + 0.5$. Such a decay is still strong for grid 2, but it starts at $s = T_r/2 + 1.5$, while it grew for $s < T_r/2 + 1.5$ during a time unit. It deserves to be remarked that the decay of the amplitude of v takes place in junction with the growth of grid spacing that starts from $x/B = 1.001$ and $x/B = 2$ respectively for grid 1 and 2. In the case of grid 3, that is refined up to $x/B = 9$, the amplitude of the perturbation grows during four time units, and then begins to decrease, but slowlier than in the other two cases. Hence, the large difference between the first two simulations and the third is obviously held against the greater diffusive error connected to the coarsening of grid 1 and grid 2 in that region of the wake.

The Figure 21 shows the effect of the numerical diffusivity on the flow simulated with grids 1 and 3 by means of the visualization of the instantaneous vorticity field in the wake. The across-wind extent of the wake simulated with grid 1 is larger than the one obtained with grid 3. In the first case the convection of the perturbation cannot be even appreciated, because it is quickly diffused by numerical effects in near wake. In

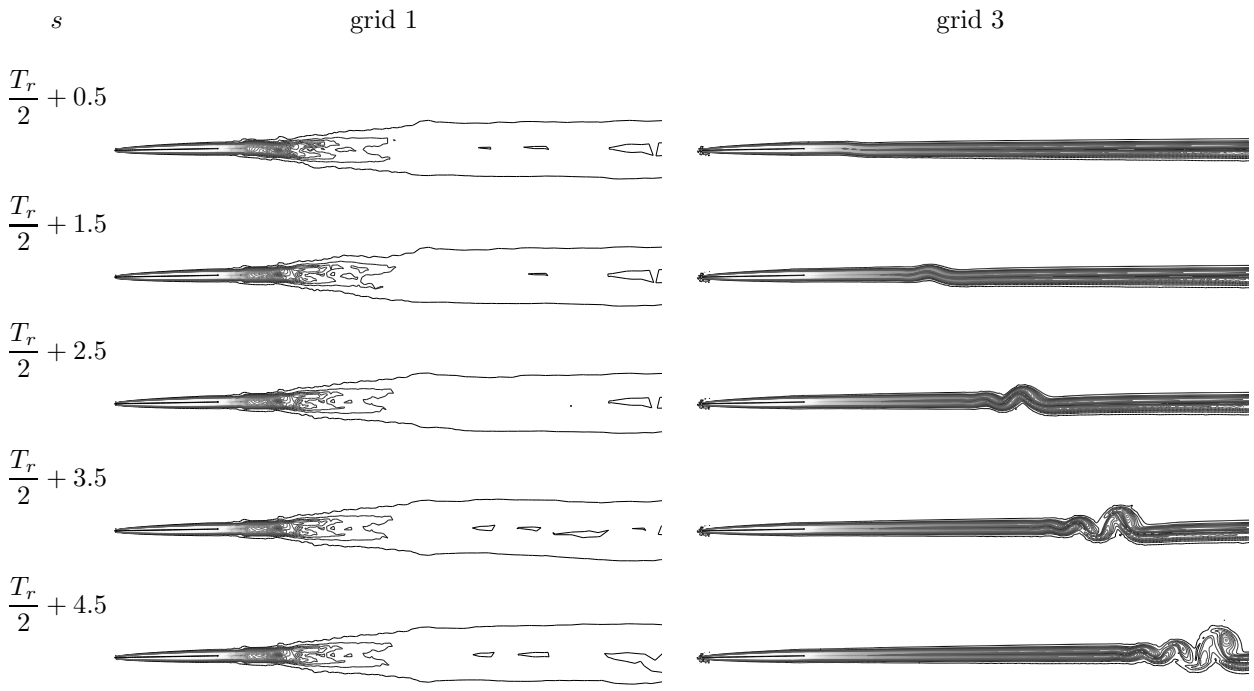

Figure 21: Vorticity magnitude field in the wake with different grid density

the second case, the convection is associated to an instability of the perturbation in the wake. The analysis of this instability is out of the scope of the present paper: herein it is enough to point out that such result doesn't seem to depend on computational errors and to conclude that the transport of the vortex is well solved only in the case of grid 3.

Finally, the effect of the accuracy in the wake region on the flutter derivatives is evaluated in Figure 22. The grid density in the wake leads to some difference at the highest reduced velocities, i.e. at the lowest frequencies and hence at the longest wave lengths. On one hand, the grid 3, solving with good accuracy

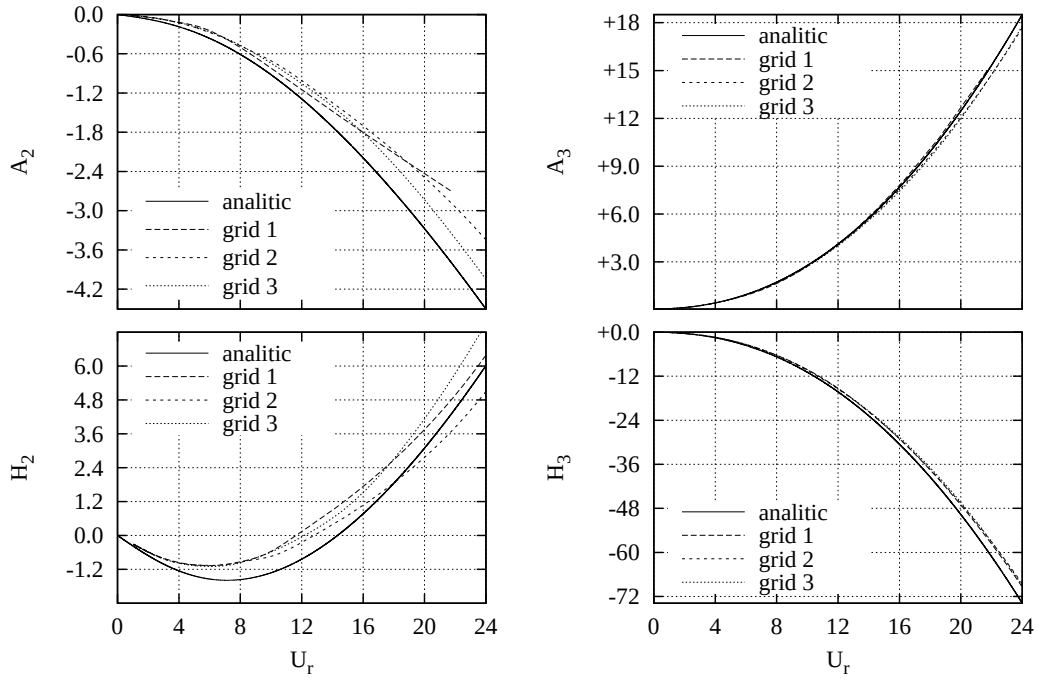

Figure 22: Flutter derivatives obtained with different grid density in the wake

the long spatial scales of the wake, shows a more regular trend of the computed A_2 and H_2 derivatives for $U_r > 10$, even if the scatter with respect the theoretical results remains. On the other hand, the derivatives A_3 and H_3 do not depend significantly on the wake discretization and the computed ones agree very well with the analytical ones at every reduced velocity.

4.6 Complete set of aeroelastic transfer functions: accuracy and costs

The complete set of 8 flutter derivatives is obtained for both the degrees of freedom θ and y by using the parameters selected above: error function, $T_r = 8.1e-1$, grid 3. The results are compared in Figure 23 with both the closed-form solution and the point-wise computational data obtained by applying the forced harmonic oscillations method [5].

From a quantitative point of view, the agreement between the present results and the analytical form

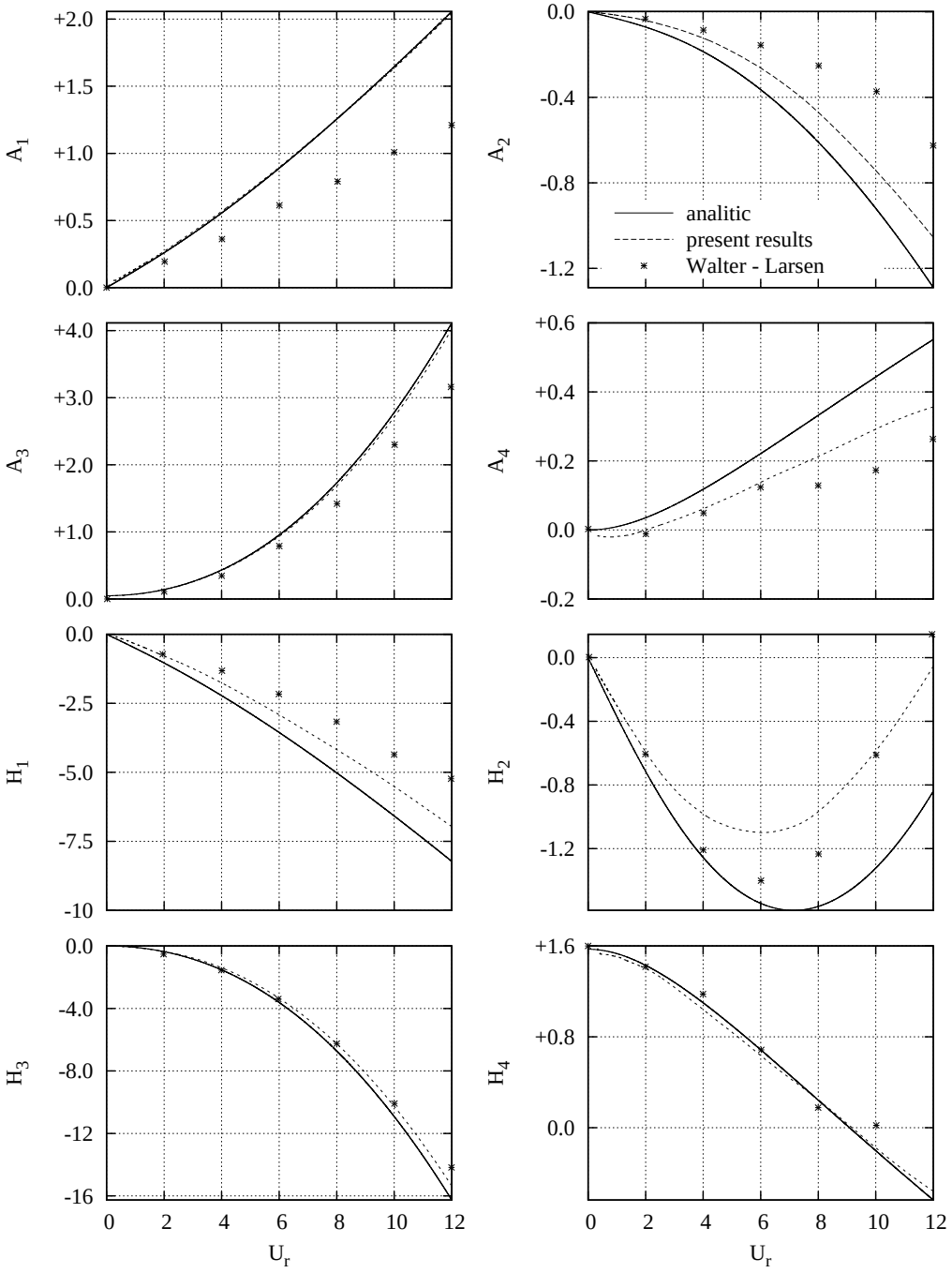

Figure 23: Complete set of flutter derivatives

ranges from excellent (A_1^*, A_3^*, H_3^* and H_4^*) to good (A_2^*, A_4^*, H_1^* and H_2^*).

The components of the Theodorsen function are obtained from the flutter derivatives by means of the well known analytical relations expressed by Simiu & Scanlan [3] and plotted in figure 24 for a wider range of reduced velocities. In particular, the real component F is recovered from the A_1^* derivative, while the

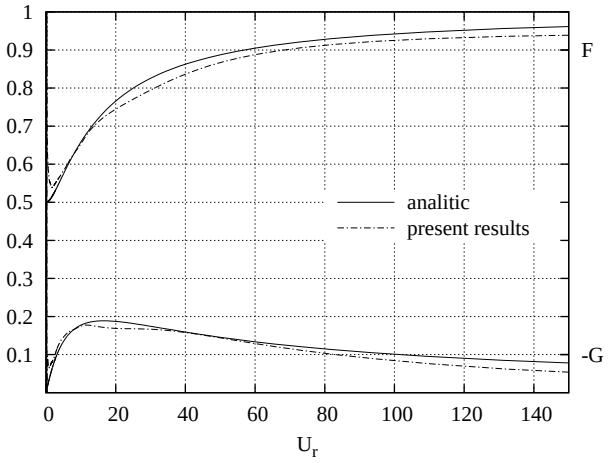

Figure 24: Comparison between analytical and computed Theodorsen function

imaginary one G is expressed as a function of H_4^* only.

Generally speaking, the obtained transfer functions show the same trend of the analytical ones: on one hand the agreement is excellent at the reduced velocities of interest for Wind Engineering; on the other hand the accuracy decreases at the highest reduced velocities. The proposed smoothed ramp approach overcomes the harmonic oscillations method in both qualitative and quantitative aspects.

Figures 25 and 26 are proposed in order to emphasize the differences between the above mentioned methods in terms of computational costs and accuracy. Referring to the costs (Fig. 25), they are expressed by the

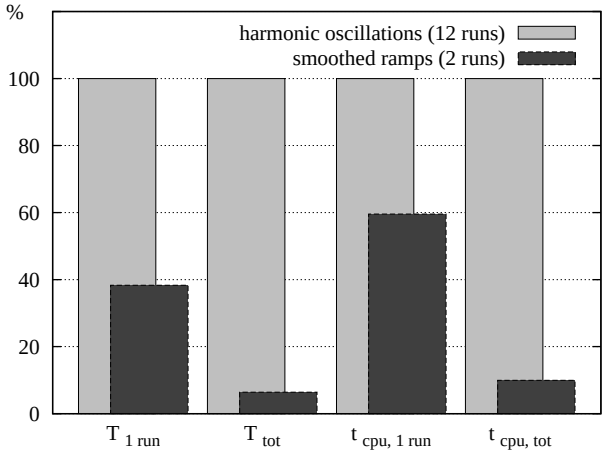

Figure 25: Comparison of the computational costs required by the harmonic oscillations method and the proposed one

ratio of both the flow times T and the cpu times t_{cpu} required for 1 simulation and the one needed to obtain the complete set of flutter derivatives.

The reduction of the flow time elapsed during one run is due to the fact that the proposed approach only needs the simulation of the transient flow, while the harmonic oscillation method discards it and requires the following periodic flow. The gain is reduced in term of cpu time because of the small time step required to discretize accurately the ramp time T_r.

Moreover, it is worth to point out that the proposed method requires only two simulations to obtain the 8 flutter derivatives at every reduced velocity. To obtain the same goal by means of interpoled point-wise

results, the harmonic oscillation method needs at least 12 simulations. Hence, the forced oscillation approach ensures a strong reduction of the total computational effort: the needed cpu time is approximatively equal to 0.1 times the one required by the harmonic oscillation method.

The results obtained by the proposed approach match more closely the analytical ones than the ones

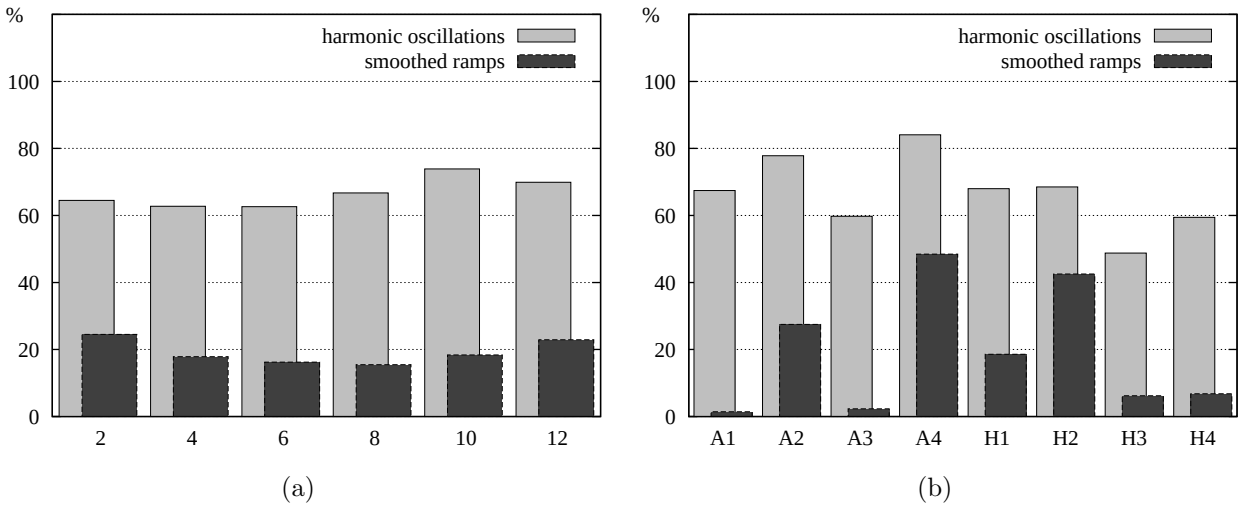

Figure 26: Comparison of the averaged scatter from the analytical solution at different reduced velocities (a) and for each derivative (b)

proposed by Walther and Larsen by using the harmonic oscillations. On one hand, the reduction of the scatter is probably due to the more accurate modeling of the flow; on the other hand, the more compact numerical post processing required to obtain flutter derivatives in the proposed approach can further reduce the errors.

Figure 26 (a) clearly shows that the scatter between the analytical results and the present ones increases as the reduced velocity does. Such a trend can be due to two different reasons. First, the coarse grid far from the obstacle in the wake ($x/B > 9$) may introduce numerical or "false" diffusivity. It follows that the flutter derivatives are generally underestimated and hence the results are really affected by an error. Then, it is worth to recall that the closed-form solution of Theodorsen assumes an inviscid and irrotational flow while the present results are obtained in case of viscous flow at high Reynolds number ($Re = 1.e + 4$). Hence, the "true" diffusive effect of the molecular viscosity on the flutter derivatives cannot be excluded *a priori* but it can be even expected. In fact, for long wavelengths or for some derivative (see Fig. 26 (b)), the viscosity may dump the perturbation introduced in the flow by the motion, it may reduce the effect of the latter on aeroelastic forces and thus it may decrease the value of the derivative.

For the above-mentioned reasons, herein the term *scatter* is preferred to *error*.

5 Conclusions

The present paper analysises the possibility of estimating the aeroelastic transfer functions, i.e. the Theodorsen function or the Scanlan's flutter derivatives, for a streamlined body through computational simulation of the flow around the moving obstacle. The classical indicial approach is modified in order to guarantee its compatibility with the computational tool. A number of studies are carried out on the mathematical and computational aspects of the approach in order to select the best ones and to discuss numerical errors.

The obtained results are in good agreement with the analytical solutions available in literature. The proposed approach guarantees more accurate results and reduced computational costs with respect to the method based on forced harmonic motion.

The conclusive results obtained on the modelling and computational aspects allow to straightforward further studies on physical parameters as the Reynolds number or the incoming turbulence intensity in view of the industrial application of the proposed approach.

Acknowledgements

The authors wish to express their grateful acknowledgment to the L3M - Laboratoire de Modélisation et Simulation Numérique en Mécanique - Marseille - France for the kind availability of the computing facilities.

The OptiFlow Company is fully acknowledged for its support.

References

[1] T. Theodorsen. General theory of aerodynamic instability and the mechanism of flutter. *NACA TR 496*, 1935.

[2] R.H. Scanlan and J.J. Tomko. Airfoil and bridge deck flutter derivatives. *J. Engrg. Mech.Div.*, (97(6)):1717–1737, 1971.

[3] E. Simiu and R.H. Scanlan. *Wind Effects on Structures: Fundamentals and Applications to Design*. John Wiley & Sons Inc, 1996.

[4] M. Matsumoto. Aerodynamic damping of prisms. *J. of Wind Engeneering and Industrial Aerodynamics*, (59):159–175, 1996.

[5] J.H. Walther and A. Larsen. Two dimensional discrete vortex method for application to bluff body aerodynamics. *J. of Wind Engeneering and Industrial Aerodynamics*, (67/68):183–193, 1997.

[6] G. Vairo. A numerical model for wind loads simulation on long-span bridges. *Simulation Modelling Practice and Theory*, (11):315–351, 2003.

[7] R.H. Scanlan O.P. Le Maître and O.M. Knio. Estimation of the flutter derivatives of an naca airfoil by means of navier-stokes simulation. *J. Fluids and Structures*, (17):1–28, 2003.

[8] Y.C. Fung. *An Introduction To The Theory Of Aeroelasticity*. Dover, New York, 1993.

[9] I.E. Garrick. On some reciprocal relations in the theory of nonstationary flows. *NACA Rrt 629*, 1938.

[10] P.S. Brar, R. Raul, and R.H. Scanlan. Numerical calculation of flutter derivatives via indicial functions. *J. of Fluids and Structures*, (10):337–351, 1996.

[11] D. Lesieutre, P. Reisenthel, and M. Dillenius. A practical approach for calculating aerodynamic indicial functions with a navier-stokes solver. *AIAA 94-0059*, 1994.

[12] J. Donea. An arbitrary lagrangian-eulerian finite element method for transient fluid-structure interactions. *Comput. Methods Appl. Mech. Engrg.*, (33):689–723, 1996.

[13] T. Nomura and T.J.R. Hughes. An arbitrary lagrangian- eulerian finite element method for interaction of fluid and a rigid body. *Comput. Methods Appl. Mech. Engrg.*, (95):115–138, 1992.

[14] L.P. Zhang and Z.J. Wang. A block lu-sgs implicit dual time-stepping algorithm for hybrid dynamic meshes. *Computers & Fluids*, (33):891–916, 2004.

[15] T. Tamura, Y. Itoh, A. Wada, and K. Kuwahara. Numerical study of pressure fluctuations on a rectangular cylinder in aerodynamic oscillation. *J. of Wind Engeneering and Industrial Aerodynamics*, (54/55):239–250, 1995.

[16] U.Y. Jeong and S.D. Kwon. Sequential numerical procedures for predicting flutter velocity of bridge sections. *J. of Wind Engeneering and Industrial Aerodynamics*, (91):291–305, 2003.

[17] H. Jasak. *Error Analisys and Estimation for the Finite Volume Method with Applications to Fluid Flows, PhD Thesis*. Imperial Colege, London, 1996.

[18] J.T. Batina. Unsteady euler airfoil solutions using unstructured dynamic meshes. *AIAA Paper*, (89-0115), 1989.

[19] C. Farhat, C. Degand, B. Koobus, and M. Lesoinne. Torsional springs for two-dimensional dynamic unstructured fluid meshes. *Comput. Methods Appl. Mech. Engrg.*, (163):231–245, 1998.

[20] R.E. Bensow and M.G. Larson. Discontinuous/continuous least-squares finite element methods for elliptic problems. *Math. Models Methods Appl. Sci.*, 15(6):825–842, 2005.

[21] D.N. Arnold and G. Awanou. Rectangular mixed finite elements for elasticity. *Math. Models Methods Appl. Sci.*, 15(9):1417–1429, 2005.

[22] R. Eymard, T. Gallouët, and R. Herbin. Finite volume methods. In *Handbook of numerical analysis, Vol. VII*, Handb. Numer. Anal., VII, pages 713–1020. North-Holland, Amsterdam, 2000.

[23] J. H. Ferziger and M. Peric. *Computational Methods for Fluid Dynamics*. Springer, Berlin, 3rd edition, 2002.

[24] H. Schlichting. *Boundary-Layer Theory*. McGraw-Hill, New York, 7th edition, 1979.

[25] S. Goldstein. On the two-dimensional steady flow of a viscous fluid behind a solid body. *Proc. Royal Society of London Series A*, pages 545–573, 1933.

[26] A. Acrivos A.S. Grove, E.E. Petersen. Velocity distribution in the laminar wake of a parallel flat plate. *The Physics of Fluid*, 1964.